Svedberg Open
DISSEMINATION OF KNOWLEDGE

International Journal of Artificial Intelligence and Machine Learning

Publisher's Home Page: https://www.svedbergopen.com/

Research Paper Open Access

AI-Assisted Measurement Choices Shape Surface Urban Heat Island Estimates: Rural Reference, Spatial Support, and Product Differences in Ahmedabad, India

Tejas Patel[1], Prachi Talsania[2], Parwathi Pillai[3*]

[1,2]Department of Environmental Engineering, Swarrnim Institute of Technology, Swarrnim startup & Innovation University, Gandhinagar 382420, India.
[3]Department of Chemical Engineering, Swarrnim Institute of Technology, Swarrnim startup & Innovation University, Gandhinagar 382420, India.
[*]Corresponding Author, Email: Parwathi.pillai@gmail.com, Parwathi.chemical@swarrnim.edu.in

Highlights

- Rural reference class alone moved the daytime SUHI by 3.03 °C and reversed its sign
- Residual Landsat–MODIS difference on a common grid exceeded the grid-size component
- At 1 km the mean SUHI is essentially unchanged while the 99th-percentile area is lost
- Tail loss matches what averaging predicts from the observed patch fragmentation
- SUHI values are comparable only if reference, support and product are all reported

Abstract

Surface urban heat island (SUHI) intensity is commonly reported as a single daytime value from one thermal product and one rural reference. Using Landsat daytime land surface temperature at 100 m and MODIS daytime and night-time LST at 1 km for the 2020 and 2025 hot seasons in Ahmedabad, India, with an urban mask defined independently of any thermal input, we varied the rural reference class, spatial support, temporal aggregation and thermal product one element at a time. Three results follow. The rural reference dominates the daytime estimate: holding epoch, product and season fixed, the 2025 daytime intensity was +2.29 °C against natural vegetation, +1.02 °C against cropland and −0.74 °C against bare and sparsely vegetated ground, a range of 3.03 °C that includes a change of sign. Aggregation attenuates different statistics at very different rates, and the contrast can be made at a single support: moving the 100 m field to 1 km leaves the mean intensity unchanged to within 2 % but retains none of the urban area exceeding the fine-grid 99th percentile. That surface occupies 4.5 km^2 in 158 patches averaging about three pixels, so its loss is close to what block-averaging must produce and quantifies fragmentation rather than revealing a new effect. Extending the rescaling to 2.9 km reduces the mean to 64 % of its fine-grid value, a decline we attribute tentatively to mixing of urban and rural land within coarse cells and do not resolve here. Placing the two products on a common 1 km grid left a mean absolute monthly difference of 1.24 °C, numerically equal to the daytime intensity being measured. Two qualifications apply. The residual is not attributable to the instrument, since overpass time, platform, retrieval, screening and compositing differ between products and were not separated; and the day–night comparisons reported here use fields of different spatial support and are not quantitative. The findings indicate that SUHI values are not comparable across studies unless the reference class, spatial support and product are reported together.

Keywords: surface urban heat island; land surface temperature; rural reference definition; spatial support; product comparability; Ahmedabad.

1. Introduction

Half a century after the first satellite observation of an urban thermal anomaly (Rao, 1972), the surface urban heat island (SUHI) has become one of the most widely reported diagnostics in urban environmental science. Its appeal is that a single differencing operation on a thermal image yields a number that appears to characterise a city. That convenience conceals a dependency structure: a reported SUHI intensity is jointly determined by the city, the thermal product used, the hour of the overpass, the season, the spatial support of the pixel and the operational definition of "rural" (Voogt and Oke, 2003; Stewart and Oke, 2012; Zhou D. et al., 2019). In temperate and humid-tropical settings these dependencies are comparatively benign, because the midday urban–rural contrast is large, positive and robust to most reasonable analytical choices (Imhoff et al., 2010; Peng et al., 2012; Clinton and Gong, 2013). The reporting convention of one daytime value, from one product, against one reference was established in exactly the climates where it is least likely to fail.

Hot arid and semi-arid cities do not satisfy those conditions. Their surroundings are bright, dry, sparsely vegetated soils with low thermal admittance and little evaporative cooling, and such surfaces warm rapidly under high solar elevation. The midday contrast between city and countryside narrows and can invert, producing a daytime surface urban cool island (Lazzarini et al., 2013; Rasul et al., 2015; Haashemi et al., 2016), while after sunset the built fabric retains energy that the open plain radiates away (Oke, 1982; Arnfield, 2003; Chow et al., 2012; Oke et al., 2017). Because thermal remote sensing samples the radiometric skin temperature of the surfaces facing the sensor rather than canopy-layer air, the surface anomaly does not share the diurnal phase of the air-temperature anomaly (Roth et al., 1989; Voogt and Oke, 2003).

1.1 What is already established for Ahmedabad

Ahmedabad is not an unstudied case, and the diurnal behaviour of its surface heat island has been documented in detail. Mohammad et al. (2019) analysed sixteen years of MODIS observations (2003–2018) over the city, in summer and winter and by day and night, and reported a mean negative SUHI during summer daytime, a slight positive value in winter daytime (0.4 °C), and clearly positive nocturnal intensities in summer (1.8 °C) and winter (3.2 °C). They attributed the negative daytime signal to the sparse vegetation of the rural surround, where croplands give way to bare soil during the pre-monsoon season, and supported the satellite result with a field campaign measuring LST at rural and urban sites in summer 2018. Mathew et al. (2022) examined thirteen years of MODIS and Landsat data over the same city and showed that the association between LST and surface descriptors differs between day and night: bareness correlated positively with LST during the day but negatively at night, while vegetation was inversely and built-up index directly related in both. At the national scale, Mathew et al. (2018) analysed diurnal surface temperature variation for SUHI assessment across Indian cities, and Mohammad and Goswami (2021) quantified diurnal and seasonal SUHI intensity and its determinants across Indian climatic zones. Related Indian work has identified vegetation cover as a dominant intra-urban control (Grover and Singh, 2015) and reproduced the dependence of the surface energy partition on land-use configuration in mesoscale simulation (Sultana and Satyanarayana, 2023). Consistent with these, Shastri et al. (2017) found daytime SUHI intensity to be negative over most Indian urban areas in the pre-monsoon season and positive at night, and Kumar and Mishra (2019) reported that Indian SUHI intensity declines during heatwaves.

The day–night contrast in Ahmedabad, the negative or weak summer daytime intensity, the nocturnal positive anomaly, and the reversal of surface-parameter associations between day and night are therefore established results, not new ones. The present study does not report them as novel, and its claims are framed accordingly.

1.2 What remains unresolved

Three limitations persist in this body of work, and they concern measurement rather than phenomenon.

First, the rural reference is treated as a fixed definition rather than as a variable. Mohammad et al. (2019) identified the composition of the rural surround as the reason for the negative daytime signal, but the sensitivity of the reported intensity to that composition has not been quantified for the city. Because national and continental analyses aggregate over cities whose surroundings range from irrigated cropland to bare desert, the axis along which the daytime sign moves is precisely the axis that aggregation conceals.

Second, spatial support and thermal product are recognised individually as sources of discrepancy (Sobrino et al., 2012; Hu and Brunsell, 2013; Zhou D. et al., 2019) but are seldom separated from one another within a single domain. Coarse and fine products differ simultaneously in grid, radiometry, overpass time, emissivity treatment, quality screening and compositing, so a Landsat–MODIS difference carries no attribution unless the grid is first held constant.

Third, the adequacy of a thermal product is normally judged by how well it reproduces a mean or a regression slope. For intra-urban prioritisation the operative property is different: whether the upper tail of the temperature distribution, carried by small and fragmented surfaces, survives aggregation. This has not been reported as an explicit criterion alongside the conventional bulk statistics.

1.3 Aim and contribution

We therefore treat Ahmedabad not as a case in which to detect a heat island but as a domain in which to measure how far a reported SUHI depends on the decisions taken while measuring it. Three questions organise the analysis. How much does the daytime intensity move when only the rural reference class changes? How do bulk statistics and threshold exceedance respond to aggregation? And how large is the difference between two thermal products once they are placed on a common grid, and what does that residual contain? A fourth question, whether daytime and night-time observations rank the same parts of the city, is not resolved by the present design. Night-time LST is available only at 1 km, and the day–night comparisons reported below are computed against the 100 m daytime field, so each confounds time of day with spatial support. They are therefore reported as secondary observations rather than as findings, and the corresponding statistics are not interpreted quantitatively.

The contribution is accordingly methodological and diagnostic rather than phenomenological. We quantify the reference-class sensitivity of the daytime estimate for a city where that sensitivity has been invoked but not measured; we report attenuation of threshold exceedance alongside attenuation of the mean and the variance, as complementary criteria for judging a product; and we partition a two-product discrepancy into a grid-size component and a residual, specifying what that residual does and does not contain. Throughout, where a result proved dependent on analytical choice we report the range of outcomes rather than a single value, and where the design cannot support an inference we say so.

2. Measurement Design As A Source Of Divergence

2.1 Support, product and definition

The reported SUHI depends strongly on how it is observed. Sobrino et al. (2012) showed that spatial resolution and overpass time both alter the evaluated effect, and Hu and Brunsell (2013) that the temporal aggregation of LST, meaning how many scenes are composited and how gaps are treated, changes the estimated intensity. Emissivity assumptions embedded in retrieval algorithms propagate systematically into Landsat-derived SUHI values worldwide (Chakraborty et al., 2021), and sub-pixel heterogeneity makes a coarse thermal pixel a nonlinear mixture rather than a simple average of the surfaces it contains (Zakšek and Oštir, 2012; Zhan et al., 2013). Definitional choices matter comparably: the delineation of urban extent and its reference class can shift intensities by degrees (Chakraborty and Lee, 2019; Li Y. et al., 2021), and surface and air-temperature heat islands are not interchangeable diagnostics (Anniballe et al., 2014; Venter et al., 2021). Reviewing this evidence, Zhou D. et al. (2019) identified the resulting incommensurability of published SUHI values as an obstacle to cumulative progress.

Two gaps follow. Scale and product are usually discussed together but estimated apart, so that a Landsat–MODIS difference carries no attribution unless the grid is held constant; data-fusion approaches address the practical need for frequent fine-resolution LST (Weng et al., 2014) without isolating what the products contribute. And product adequacy is judged by reproduction of a mean, although for intra-urban prioritisation the operative property is whether the extreme upper tail survives aggregation.

2.2 Attribution and its statistical difficulties

Explanations of why some urban surfaces are hotter than others typically regress LST on surface descriptors such as vegetation indices, imperviousness, albedo, building metrics and population (Li J. et al., 2011; Zhou D. et al., 2014; Bounoua et al., 2015; Zhou B. et al., 2017; Xia et al., 2022). Thermal fields are strongly spatially autocorrelated, so ordinary standard errors computed over millions of pixels are severely anti-conservative and nominal significance is effectively guaranteed. Broad-scale predictors such as background climate and population are well established as determinants of SUHI magnitude between cities (Zhao et al., 2014; Manoli et al., 2019; Liu et al., 2022), but they operate across cities and are silent about the within-city geography that intervention requires. Where night-time controls have been examined, as in the sub-tropical diurnal analysis of Chakraborty et al. (2017) or the seasonal hysteresis documented by Yang and Zhao (2023), the emphasis has been on temporal trajectories rather than on the comparability of day and night estimates obtained at different spatial supports.

A further disconnection is institutional. Heat action plans allocate resources through administrative units such as wards and zones (Knowlton et al., 2014; Hess et al., 2018), whereas thermal analyses report pixels or radial profiles. Whether daytime and night-time observations identify the same units, and whether such a comparison is meaningful when the two observations differ in spatial support, is rarely tested.

3. Study Area And Data

3.1 Study area

Ahmedabad (23.03° N, 72.58° E) lies on the alluvial plain of the Sabarmati river in Gujarat, western India, and is the largest urban agglomeration in the state. Its climate is hot semi-arid (Köppen BSh), organised around a long and intense pre-monsoon season from March to June, a monsoon that arrives in late June, and a short mild winter. Two features make the site suitable for the present purpose. The terrain is flat, which limits elevation as a confounder of the urban–rural contrast. And the city operates an evaluated heat-health action plan (Knowlton et al., 2014; Hess et al., 2018), so that the measurement choices examined here bear on decisions that are actually taken.

The analysis domain is the city's functional urban area (Dijkstra et al., 2019) extended by a 10 km buffer, giving a fixed footprint of 3,770 km^2 (Fig. 1a) applied identically to both epochs so that no part of the epoch comparison reflects a change in the region analysed. Within this domain the surrounding landscape is predominantly cultivated rather than desert: cropland accounts for 67.9 % of the area and built-up land for 13.3 % (503 km^2), with tree cover at 12.2 % and smaller fractions of shrub, grassland, bare ground and water.

This composition matters for the interpretation of every daytime result reported below, because an irrigated cropland reference and a bare-soil reference sit at opposite ends of the range over which the daytime SUHI sign is known to move (Shastri et al., 2017; Kumar and Mishra, 2019).

3.2 Observational design

Rather than reporting a single intensity, we vary the elements that a conventional SUHI estimate holds fixed, changing one at a time (Fig. 2). Six factors are varied: time of day (day, night); epoch (2020, 2025); thermal product (Landsat, MODIS); spatial support (100 m to approximately 2.9 km); temporal aggregation (April, May, June and the April–June composite); and rural reference class (all non-built land, cropland only, natural vegetation only, bare and sparsely vegetated ground only). A full crossing of these factors is not observationally available, because night-time LST exists only at 1 km and Landsat supplies no night-time acquisition for this domain. Factors are therefore varied in nested groups such that each comparison isolates one element while the remainder are held fixed. One consequence should be stated at the outset: daytime and night-time observations are not available at a common support, so any direct day–night comparison of spatial pattern in this study carries a difference in support as well as in time of day.

3.3 Land surface temperature

Two thermal sources were used, selected so that spatial resolution and time of day can be varied independently (Table 1). Daytime LST at 100 m was obtained from Landsat 8 and 9 thermal infrared observations, which cross the equator at approximately 10:30 local solar time. The 100 m grid corresponds to the native acquisition resolution of the thermal instrument rather than to the 30 m grid on which Landsat products are commonly distributed. This distinction matters here because the fine-grid percentile thresholds and the patch sizes discussed in Section 5.4 are defined on that grid, and thresholds defined on resampled 30 m data would describe a different set of surfaces. Day and night LST at 1 km were obtained from MODIS observations acquired by Terra and Aqua. Both sources were composited identically as per-pixel medians for April, May and June separately and for the April–June season as a whole, the median being preferred to the mean for its insensitivity to residual undetected cloud and to sensor artefacts. The retrieval chains behind the two products differ in ways that matter for their comparison: MODIS land surface temperature derives from a generalised split-window algorithm with classification-based emissivity, refined and validated in Collection 6 (Wan, 2014; Duan et al., 2019), whereas Landsat surface temperature rests on single-channel inversion with atmospheric compensation from reanalysis profiles (Malakar et al., 2018), and its accuracy is sensitive to the emissivity model adopted (Sekertekin and Bonafoni, 2020). Both approaches are reviewed by Li Z.-L. et al. (2013), and open implementations for the Landsat archive are available in cloud-based processing environments (Gorelick et al., 2017; Ermida et al., 2020). These differences are among the reasons the residual term of Section 4.4 cannot be interpreted as an instrument effect alone.

All products were expressed in degrees Celsius on a common geographic grid (EPSG:4326). At the latitude of the domain a nominal 100 m pixel measures 99.3 m north–south by 92.0 m east–west, and this anisotropy is carried explicitly through every area and distance calculation rather than approximated. Valid-pixel coverage exceeds 99 % in all products and months except June, when monsoon cloud reduces Landsat coverage to 94–96 %; the seasonal composites are complete. Analysis is restricted to April–June, the period in which the pre-monsoon surface is driest and heat constitutes an acute health hazard.

Because the nominal overpass times of the two platforms differ, with Terra near 10:30 and 22:30 local time and Aqua near 13:30 and 01:30, the platform composition determines what "day" and "night" denote in the MODIS composites. Landsat and MODIS also differ in spectral configuration, emissivity retrieval, atmospheric correction, quality screening and the number of valid acquisitions contributing to each composite. Their difference is therefore a compound quantity, and Section 4.4 separates from it only the component attributable to nominal grid size. Because no thermal sensor supplies night-time LST at 100 m over this domain, the fine spatial structure of the nocturnal field is not directly observable; night-time results are reported at their native 1 km support throughout and no downscaling is performed (cf. Zakšek and Oštir, 2012; Zhan et al., 2013).

We note two reproducibility limitations of the present description. Product collection identifiers, per-month counts of valid acquisitions, quality-flag settings and cloud-shadow screening rules are not reported here, and the urban mask for the later epoch derives from the most recent available WorldCover release rather than from a product contemporaneous with 2025. These details are required for full reproduction and are listed among the items for deposition in the data availability statement.

3.4 Surface-property and ancillary data

Urban and rural masks were derived from the ESA WorldCover built-up class (class 50), resampled to the 100 m analysis grid and applied separately to each epoch (Zanaga et al., 2021, 2022). The mask lineage is deliberately independent of any thermal input, so that the SUHI is never defined, even indirectly, by the quantity it is intended to measure, a circularity that affects thermally derived urban extents (Chakraborty and Lee, 2019).

Seven surface-property predictors were assembled at 100 m for both epochs: the normalised difference vegetation index and surface albedo derived from Sentinel-2; building presence and building height from a

global building-footprint layer; tree-canopy height from a global canopy-height product; surface-water occurrence from the JRC Global Surface Water dataset (Pekel et al., 2016); and gridded population from the Global Human Settlement Layer (Schiavina et al., 2023; Pesaresi et al., 2024). As an independent check on the urban delineation we additionally used the texture-derived GHS-BUILT-S built-surface fraction (Pesaresi and Politis, 2023), which shares no processing lineage with the WorldCover classification.
Administrative geography was represented by the 48 wards of the Ahmedabad Municipal Corporation (AMC), covering 438 km^2, rasterised onto the 100 m analysis grid.

3.5 Meteorological context

Independent meteorological context was taken from the ERA5 reanalysis (Hersbach et al., 2020), from which we extracted summer mean air temperature, mean heat index, and annual counts of days falling in each NOAA heat-index category. The heat index follows the standard apparent-temperature formulation grounded in the physiological work of Steadman (1979) and implemented as described by Anderson et al. (2013). ERA5 serves strictly as an external, non-satellite reference against which the interannual behaviour of the thermal fields can be checked; it is not used in the computation of any SUHI value.

Table 1. Inventory of thermal, surface-property and meteorological datasets. Native resolution refers to the product as supplied; the analysis grid is the support at which each variable enters the calculations reported here. Local overpass times are nominal.

Variable	Source	Native resolution	Local overpass	Temporal aggregation	Use in this study
Daytime LST	Landsat 8 and 9	100 m	≈10:30	Median: Apr, May, Jun, Apr–Jun	Primary daytime field; scale ladder; driver attribution
Daytime LST	MODIS (Terra and Aqua)	1 km	≈10:30 and 13:30	Median: Apr, May, Jun, Apr–Jun	Cross-sensor comparison at matched time of day
Night-time LST	MODIS (Terra and Aqua)	1 km	≈22:30 and 01:30	Median: Apr, May, Jun, Apr–Jun	Primary night-time field; ward analysis
Land cover, urban/rural mask	ESA WorldCover (Zanaga et al., 2021, 2022)	10 m, used at 100 m	—	Per epoch	Urban and rural sampling; reference-class variants
Built-surface fraction	GHS-BUILT-S (Pesaresi and Politis, 2023)	100 m	—	Per epoch	Independent check on urban delineation
NDVI, albedo	Sentinel-2	100 m	—	Seasonal composite	Driver attribution; hot-spot composition
Building presence, building height	Global building-footprint layer	100 m	—	Per epoch	Driver attribution; hot-spot composition
Tree-canopy height	Global canopy-height product	100 m	—	Static	Driver attribution; hot-spot composition
Surface-water occurrence	JRC Global Surface Water (Pekel et al., 2016)	30 m, used at 100 m	—	Long-term	Water exclusion; driver attribution
Gridded population	GHS-POP (Schiavina et al., 2023)	100 m	—	Per epoch	Population on hot-spot surfaces
Ward boundaries	Ahmedabad Municipal	Vector, rasterised at 100 m	—	Static	Zonal statistics; spatial clustering

Variable	Source	Native resolution	Local overpass	Temporal aggregation	Use in this study
	Corporation, 48 wards				
Air temperature, heat index	ERA5 (Hersbach et al., 2020)	≈31 km	Hourly	Seasonal mean; annual day counts	Independent meteorological context only

4. Methods

4.1 Definition of surface urban heat island intensity

For a given sensor s, epoch e and temporal aggregation t, surface urban heat island intensity is the difference between the mean land surface temperature of urban pixels and that of rural pixels within the fixed domain:

$$SUHII_{s,e,t} = (1/N_U)\ \Sigma_{i\in U}\ T_{s,e,t}(i) - (1/N_R)\ \Sigma_{j\in R}\ T_{s,e,t}(j) \tag{1}$$

where U is the set of urban pixels, R the set of rural pixels, and N_U, N_R their cardinalities. Urban pixels are those classified built-up; rural pixels are all non-built, non-water land within the same footprint. Permanent water, wetland and mangrove classes are excluded from both samples, so that neither the Sabarmati nor the reservoirs within the domain can bias the contrast through the strong thermal signature of open water.

Analyses that require a spatially compact city, specifically the thermal-footprint calculation of Section 4.6, use a contiguous urban core rather than the full built mask, because a simple distance-to-edge measure is not meaningful in a landscape threaded with villages and road corridors. The core is defined as the union of connected built patches of at least 25 km²; it covers 219 km², approximately half of all built land in the domain, and its largest single component is 128 km².

4.2 Epoch comparison on stable masks

To ensure that no part of the 2020–2025 difference reflects a change in land-cover labelling rather than a change in temperature, all epoch comparisons are computed on stable masks, the intersections of the two epochs' classifications:

$$U* = U_{2020} \cap U_{2025}, \quad R* = R_{2020} \cap R_{2025} \tag{2}$$

The thermal change is thus evaluated on a fixed set of ground whose classification did not alter between epochs. We emphasise that two epochs support a statement about interannual difference, not about trend, and the results are framed accordingly throughout.

4.3 Uncertainty under spatial dependence

Adjacent thermal pixels are strongly correlated, so a conventional standard error, which presumes independent observations, would be smaller than the true sampling uncertainty by orders of magnitude on a domain of this size. We therefore quantify uncertainty by a spatial block bootstrap. The block bootstrap originates with Künsch (1989) for dependent sequences; the two-dimensional case used here follows the treatment of spatially dependent data given by Lahiri (2003). The domain is partitioned into non-overlapping square tiles of 50 pixels (approximately 5 km) at 100 m support and 5 pixels at 1 km support. Tiles are drawn with replacement to reconstitute a domain of the original size, each tile carrying its constituent pixels together with their urban or rural class membership, so that the urban–rural contrast is recomputed on each replicate from whichever pixels the resampled tiles contain. The statistic is recomputed on each of B = 1,000 replicates.

Three properties of this scheme bound what the resulting intervals mean, and we state them rather than leave them implicit. First, the precision of a block bootstrap rests on the resampled units being approximately independent, which requires the tile to be large relative to the correlation length of the field. The 5 km tile is a pragmatic choice, and the residual autocorrelation reported in the supplementary material is consistent with a correlation range that may be of the same order. Where the range approaches or exceeds the tile, the tiles are not independent and the intervals are correspondingly narrow. The intervals reported here should therefore be read as lower bounds on the true sampling uncertainty. Second, the effective sample size is the number of tiles, not the number of pixels: a 3,770 km² domain divided into 25 km² tiles yields about 151 of them, and since built land occupies 503 km², only the minority of tiles intersecting the urban class contribute to the urban mean. The degrees of freedom underlying every interval reported here are therefore of order a hundred or fewer, not of order the pixel count. Third, resampling with replacement can produce replicates in which few tiles contain urban pixels, so that the urban mean is estimated from a small and unrepresentative sample; such replicates are retained rather than discarded, which widens the interval and renders it asymmetric. The reported 95 % interval is the 2.5th to 97.5th percentile of the resulting distribution:

$$CI_{95\%} = [\ Q_{0.025}(SUHII*_{1..B}),\ Q_{0.975}(SUHII*_{1..B})\ ] \tag{3}$$

The same procedure was applied to the SUHI intensities for which intervals are reported in Section 5. Because the block bootstrap accommodates dependence within blocks but not between them, the intervals should be read as substantially more conservative than nominal standard errors while still not fully accounting for long-range spatial structure.

4.4 Separating the grid-size component from the residual product difference

To separate the influence of nominal grid size from everything else that differs between two thermal products, we construct a three-level ladder: Landsat at its native 100 m grid (L100); Landsat block-averaged onto the MODIS 1 km grid (L1K); and MODIS at 1 km (M1K). The first step changes the grid while holding the product constant; the second changes the product while holding the grid constant. The total discrepancy partitions exactly:

$$\Delta_{total} = \mathrm{SUHII(M1K)} - \mathrm{SUHII(L100)} \quad (4)$$

$$\Delta_{grid} = \mathrm{SUHII(L1K)} - \mathrm{SUHII(L100)}, \quad \Delta_{residual} = \mathrm{SUHII(M1K)} - \mathrm{SUHII(L1K)} \quad (5)$$

$$\Delta_{total} = \Delta_{grid} + \Delta_{residual} \quad (6)$$

The identity in Eq. (6) holds by construction, so the partition is exact; what is estimated is the relative size of the two terms. One property of Δ_{grid} should be recognised before it is used as a denominator. Block-averaging preserves the area-weighted mean of a field over a fixed set of cells, so if the urban and rural sets are held fixed and the cells tile the domain completely, both class means are unchanged and Δ_{grid} vanishes identically. Any departure from zero therefore reflects only incomplete cells at class boundaries and unequal cell weighting, and Δ_{grid} is expected to be small a priori rather than as an empirical finding. The ratio ρ defined below is reported for completeness but is not used as a headline result, for the reason set out in Section 5.5. L1K and M1K, constructed here for the product comparison, also constitute a daytime field on the night-time grid. The day–night comparisons of Sections 4.5 and 4.8 are computed on the native 100 m daytime field and are qualified accordingly. Their ratio is summarised as

$$\rho = \langle|\Delta_{residual}|\rangle \,/\, \langle|\Delta_{grid}|\rangle \quad (7)$$

with the average taken over the six month–epoch combinations. Pixel-level agreement between L1K and M1K is additionally reported as a Pearson correlation on the common grid, which distinguishes a systematic offset from a loss of spatial correspondence.

The interpretation of $\Delta_{residual}$ requires care, and we state its content explicitly. It is the difference remaining between two products after the nominal grid size has been equalised, and it therefore contains, in unseparated combination: differences in overpass time between Landsat and the MODIS platforms; the composition of Terra and Aqua observations within the MODIS composites; differences in LST retrieval algorithm and emissivity treatment; atmospheric correction; cloud and quality screening; viewing geometry and its effect on effective emitted radiance; the number and timing of valid acquisitions entering each composite; and any residual mismatch introduced by block averaging onto a grid whose cells are not exactly co-registered with the coarse product. We refer to it throughout as the residual product difference on a common grid, and we do not attribute it to the instrument. The residual is therefore a compound quantity, and no part of it is attributed to the instrument.

Separately, we walk a continuous scale ladder on the Landsat field from 100 m to approximately 2.9 km by successive block averaging, and track three quantities as functions of pixel size k: the SUHI intensity itself; the retention of intra-urban thermal texture,

$$\eta_\sigma(k) = \sigma_U(k) \,/\, \sigma_U(k_0) \quad (8)$$

where σ_U is the standard deviation of LST over urban pixels, k_0 = 100 m, and T_0 denotes the field at that finest support; and the retention of the hot tail,

$$\eta_A(p, k) = A\{\, T_k > \tau_p \,\} \,/\, A\{\, T_0 > \tau_p \,\} \quad (9)$$

where τ_p is the p-th percentile of the urban LST distribution at the finest support. The threshold τ_p is held fixed at its 100 m value across all k, so that η_A measures how much of the surface identified as extreme in the fine-resolution field still exceeds that same absolute threshold after aggregation.

Two properties of this measure should be recognised. It is a threshold-exceedance statistic, not a test of whether the locations of the warmest areas can still be identified: a coarse field may fail to exceed a fine-grid threshold while still ranking the same places highest. The results in Section 5.4 are accordingly described as attenuation of threshold exceedance, and no claim is made about detectability in the stronger sense. The mean intensity is available at 1 km as the grid-size component of Eq. (5), so it can be compared with η_A at that support directly; η_σ was computed only at 2.9 km and is reported separately. At coarse support η_A is quantised in units of one cell, giving a resolution of about 1 km^2 at the 1 km grid.

4.5 Hot-spot delineation and day–night congruence

Daytime and night-time hot spots were delineated as the urban surface exceeding a common percentile of the respective temperature distribution, and their spatial correspondence quantified by the Jaccard index:

$$J = |H_{day} \cap H_{night}| \,/\, |H_{day} \cup H_{night}| \quad (10)$$

We report J for the hottest quintile and, separately, the resident population located within the 90th-percentile hot surfaces of each period, obtained by summing the gridded population raster over those masks.

This comparison carries an important qualification. The daytime hot spots derive from Landsat at 100 m and the night-time hot spots from MODIS at 1 km, so the two masks differ in spatial support as well as in time of day, and J consequently confounds the two. A defensible day–night overlap statistic requires the daytime field on the night-time grid, with identical alignment, urban mask and valid-data area, hot spots defined by equivalent percentile or area criteria, and sensitivity to threshold and grid origin examined. The statistics reported in Section 5.6 are computed on fields of differing support, and are therefore an indication that the two observations rank different surfaces highly rather than a quantitative measure of congruence.

4.6 Thermal footprint

The spatial extent of the warm anomaly was measured by computing, for concentric distance bands outward from the edge of the contiguous urban core, the band-mean day and night LST, using true ground distances that respect the latitude-dependent pixel geometry. The far-field background T_{bg} is the mean of all bands beyond 15 km, and the decay distance is the first band at which the profile falls within an absolute threshold of that background:

$$d* = \min\{ d : |\bar{T}(d) - T_{bg}| \leq 0.5\ °C \} \tag{11}$$

Two properties of Eq. (11) limit its use. It is not amplitude-normalised: a fixed 0.5 °C criterion represents a different fraction of the anomaly for a day profile of amplitude 1.4 °C than for a night profile of amplitude 4.7 °C, so decay distances computed this way are not directly comparable between the two. And a first-crossing rule is ill-posed on a profile that is not monotonic, since a shallow profile that wanders near the threshold can cross it at a distance that shifts substantially under small perturbations; T_{bg} is itself an estimate carrying sampling error, which compounds this. Decay distances obtained under Eq. (11) are therefore reported as descriptive quantities, and Section 5.6 interprets the profiles through their amplitude and fitted decay scale instead. Where the comparison matters we interpret the profiles in terms of amplitude and shape rather than by d∗ alone. This defect is not carried by an amplitude-normalised criterion of the form $d*_\alpha = \min\{ d : (\bar{T}(d) - T_{bg}) / (\bar{T}(0) - T_{bg}) \leq \alpha \}$, or a parametric description of the anomaly surface of the kind used by Keeratikasikorn and Bonafoni (2018), which characterises extent through a fitted shape rather than a threshold crossing.

4.7 Attribution of the thermal field to surface properties

The daytime and night-time fields were also regressed on seven standardised surface predictors, with residual spatial autocorrelation, collinearity and a thinned-sample refit assessed as diagnostics, and the composition of the daytime thermal extremes summarised by a non-parametric dominance measure. Because the specification does not adequately represent the spatial structure of the residuals and the accompanying diagnostics are incomplete, these results are not presented among the findings of this paper. The full specification, the estimating equations and the results are given in Supplementary Section S2, and are described there as exploratory.

4.8 Ward-level aggregation and spatial clustering

To bring the analysis to the unit at which intervention is organised, per-ward means of daytime (Landsat) and night-time (MODIS) LST and of each predictor were computed by zonal aggregation over the 48 AMC wards. Ward night-time LST inherits the 1 km native support of MODIS and is consequently smoother than the daytime field. This asymmetry is stated wherever ward-level day and night results are compared, and no claim is made about night-time structure below the 1 km scale. The ward-level day–night comparison in Section 5.7 therefore contrasts fields of different spatial support, and is reported with that qualification.

Spatial clustering of ward heat was tested using queen-contiguity spatial weights, row-standardised, under which wards sharing any boundary are neighbours. Global clustering was measured by Moran's I,

$$I = (n / S_0) \cdot [\Sigma_i \Sigma_j w_{ij}(y_i - \bar{y})(y_j - \bar{y})] / \Sigma_i(y_i - \bar{y})^2, \quad S_0 = \Sigma_i \Sigma_j w_{ij} \tag{12}$$

with inference from 9,999 conditional permutations. Local clusters were identified by the local Moran statistic (Anselin, 1995),

$$I_i = [(y_i - \bar{y}) / m_2] \Sigma_j w_{ij}(y_j - \bar{y}), \quad m_2 = \Sigma_i(y_i - \bar{y})^2 / n \tag{13}$$

classified as high–high, low–low, high–low or low–high, and cross-checked against the Getis–Ord Gi∗ statistic (Getis and Ord, 1992),

$$G*_i = [\Sigma_j w_{ij} y_j - \bar{y} \Sigma_j w_{ij}] / (S \sqrt{\{ [n \Sigma_j w_{ij}^2 - (\Sigma_j w_{ij})^2] / (n - 1) \}}) \tag{14}$$

Because a local statistic is computed for every ward, the resulting p-values constitute a multiple-comparison problem with dependent tests; significance is therefore assessed after false-discovery-rate control following the procedure of Caldas de Castro and Singer (2006), which is designed for this setting. Identifying significant clusters separately in the daytime and night-time maps does not by itself establish that the two differ: a formal statement of difference would require a direct test on the day–night contrast rather than a comparison of two independently thresholded maps. We therefore describe the two maps as displaying different spatial configurations. Permutation p-values are reported at the resolution the permutation count supports; with 9,999 permutations the smallest attainable value is 1×10^{-4}, and results are reported as $p \leq 0.001$ rather than as an exact zero.

4.9 Robustness across analytical choices

Because a single-city SUHI is sensitive to arbitrary methodological decisions, the daytime and night-time intensities were recomputed under twenty alternative specifications varying the urban class, the rural reference, the handling of water and wetland, the epoch of the land-cover mask and the treatment of outlying values. The full specification list and the estimate returned by each are given in the supplementary material. The proportion of specifications returning a positive estimate describes the set of choices tested; it is not a probability that the underlying quantity is positive, and the specifications are neither equally weighted nor independent.

4.10 Software and reproducibility

Satellite compositing and zonal computation were performed in Google Earth Engine (Gorelick et al., 2017). Every quantitative claim in the Abstract and Results is traceable to a named field in a machine-readable results file; the mapping is given as Supplementary Table S1.

5. Results

5.1 Diurnal contrast in the two years analysed

In the 2025 hot-season composite, built land was 3.38 °C warmer than rural land at night (MODIS, 95 % CI 2.87–3.76) and 1.34 °C warmer by day on the same product, a night-to-day ratio of 2.5 (Fig. 3; Table 2). The independent Landsat estimate of the daytime intensity at 100 m, +1.24 °C (95 % CI 0.80–1.73), agrees with the MODIS daytime value to within 0.10 °C. Urban land cooled to 26.7 °C after dark while rural land fell to 23.3 °C. These values are consistent in direction with what has previously been reported for Ahmedabad from longer MODIS records (Mohammad et al., 2019) and for Indian cities more generally (Shastri et al., 2017; Mohammad and Goswami, 2021), and we present them as context for the measurement analysis that follows rather than as new findings. The magnitudes differ from earlier work: Mohammad et al. (2019) reported a summer nocturnal intensity of 1.8 °C and a negative summer daytime intensity over 2003–2018, whereas the present composites give +3.38 °C at night and a positive daytime value. Section 6.2 considers how far the definitional choices examined here account for that difference.

5.2 The two years produced similar point estimates

The night-minus-day contrast was +2.07 °C in 2020 and +2.04 °C in 2025 (Table 2), a difference of 0.03 °C between the two composites. Between the same epochs the mean daytime LST of the built core fell by approximately 4.1 °C, while the daytime SUHI intensity changed by +0.44 °C and the night-time intensity by +0.42 °C. A shift of 4.1 °C is large for a seasonal median, and its origin cannot be established from the present reporting: it is consistent with a genuine difference in surface conditions between the two seasons, but also with a difference in the number, dates and clear-sky character of the acquisitions entering each composite. Per-month valid-acquisition counts and dates for both products are required to separate the two, and are not reported here. Independent reanalysis indicates that 2020 was the warmer season: ERA5 recorded 117 heat-index danger-days and 109 heatwave days in 2020 against 45 and 38 in 2025.

We report these as similar point estimates and draw no inference of stability from them. Two composites, each aggregating a modest number of acquisitions, cannot establish that the day–night contrast is a persistent property of the city. A confidence interval for the difference between epochs was not computed, and doing so would require propagating the temporal sampling uncertainty of the individual acquisitions entering each composite; additional years between 2020 and 2025 would be needed to test persistence directly. The agreement to 0.03 °C is therefore a description of two numbers, not evidence of reproducibility or invariance.

5.3 The rural reference class dominates the daytime estimate

Holding epoch, product and season fixed and varying only the class of land treated as rural, the 2025 daytime intensity was +1.02 °C against cropland, +2.29 °C against natural vegetation and −0.74 °C against bare and sparsely vegetated ground (Fig. 4a; Table 2). The range of 3.03 °C spans zero, so the sign of the reported daytime heat island in this city is determined by a definitional decision rather than by the thermal field.

Season contributes a comparable dependence. In May 2020 the built core was 1.26 °C cooler than its rural surroundings, the bare pre-monsoon plain having reached 53.3 °C while the partly vegetated built core reached 52.1 °C. Across twenty analytical specifications differing in urban class, rural reference, water handling, mask epoch and outlier treatment, the daytime estimate ranged from −0.7 to +2.6 °C and was positive in 95 % of specifications, while the night-time estimate ranged from +2.8 to +3.9 °C and was positive in all of them (Fig. 4b). The proportion of positive specifications describes the set of choices tested and is not a probability that the underlying quantity is positive; the specification list is given in the supplementary material.

This result gives quantitative form to an explanation previously offered qualitatively. Mohammad et al. (2019) attributed the negative summer daytime SUHI of Ahmedabad to the cropland-to-bare-soil transition of the rural surround. Our domain is 67.9 % cropland, and against cropland the city is warmer, whereas against bare ground it is cooler. The composition of the reference class is therefore sufficient to move the estimate across zero, which is consistent with their interpretation and quantifies the sensitivity involved.

Table 2. Surface urban heat island intensity (urban minus rural mean land surface temperature, °C) on stable masks. Values for 2020 are obtained from the 2025 values and the reported epoch

differences. Confidence intervals are the 2.5th and 97.5th percentiles of a spatial block bootstrap with B = 1,000 replicates.

Estimate	Landsat day, 100 m	MODIS day, 1 km	MODIS night, 1 km
2020 April–June composite	+0.80	+0.89	+2.96
2025 April–June composite	+1.24 (0.80 to 1.73)	+1.34	+3.38 (2.87 to 3.76)
Change, 2020 to 2025	+0.44	—	+0.42
Night minus day, 2020	—	+2.07	—
Night minus day, 2025	—	+2.04	—
Urban / rural LST, 2025 composite	—	—	26.7 / 23.3 °C
May 2020 (month of sign reversal)	−1.26 (urban 52.1, rural 53.3)	—	—
2025 composite, cropland reference	+1.02	—	—
2025 composite, natural-vegetation reference	+2.29	—	—
2025 composite, bare / sparse reference	−0.74	—	—
Range across 20 analytical variants	−0.7 to +2.6 (95 % positive)	—	+2.8 to +3.9 (all positive)

5.4 Aggregation preserves the mean and removes the tail, at a common support

The two halves of this result can be compared at a single spatial support, and we do so first because that comparison is the cleanest the design permits. Moving the 100 m Landsat field onto the 1 km grid changes the mean intensity by +0.02 °C, averaged over the seasonal composites, which is the grid-size component of Eq. (5). Against a fine-grid intensity of +1.24 °C this is a change of under 2 %, so the mean is to that precision unaltered by the rescaling. Evaluated on the same 1 km field with thresholds held at their 100 m values (Eq. 9), the urban area exceeding the 90th percentile falls from 45 to 21.9 km^2, a retention of 49 %; that above the 95th percentile falls from 22 to 8.2 km^2, a retention of 37 %; and that above the 99th percentile falls from 4.5 km^2 to zero (Fig. 5a; Table 3). At one and the same support, therefore, the mean intensity is essentially preserved while the extreme tail is removed entirely.

One qualification attaches to this comparison. The grid-size term is a mean over the two seasonal composites, whereas the exceedance terms are computed for the 2025 composite alone, so the two are matched in support but not in epoch. The epoch-averaged change is 0.02 °C against a signal of 1.24 °C, so any epoch-specific departure would have to be an order of magnitude larger than the mean to affect the comparison.

Extending the rescaling to approximately 2.9 km reduces the mean intensity to +0.79 °C, a retention of 64 %, and leaves 67 % of the intra-urban standard deviation. This raises a question the present analysis cannot settle. A tenfold increase in linear pixel size costs nothing in the mean, whereas a further factor of 2.9 costs a third of it, which is not the behaviour of a smoothly degrading statistic. The most likely explanation is mixing of the urban and rural classes: as cells grow, an increasing share of them contain both, the two class means converge, and their difference contracts. If that is the cause, the decline beyond 1 km measures degradation of the urban mask rather than of the thermal field, and the two supports are not measuring the same thing. A second possibility is that the two analyses aggregate or re-derive class membership differently, in which case they should not be read as a single curve. We report the values as computed, flag the discontinuity, and identify the fraction of mixed cells as a function of support as the diagnostic that would distinguish the two explanations. The matched-support comparison at 1 km is unaffected by this question, which is why it is stated first.

The complete loss of the 99th-percentile surface should be read against what block-averaging must produce. That surface occupies 4.5 km^2 in 158 separate patches, a mean patch of about 28,500 m^2. At the pixel geometry of this domain a 100 m cell covers 9,136 m^2, so the mean patch is roughly three fine pixels, and a 1 km cell holds about 110 of them; the patch therefore occupies some 2.9 % of a coarse cell. For an unweighted mean over complete cells, the cell value is the local background plus the patch excess weighted by that areal fraction, so a patch surviving the original threshold after averaging would need to exceed its surroundings by the inverse of the fraction, about thirty-five times the margin separating threshold from background.

That factor depends on what the rest of the cell contains. Thirty-five applies when the remainder of the cell sits at the far-field background. With residual spatial autocorrelation as high as is observed here, the neighbourhood of a 99th-percentile patch is itself warm, and the required excess falls accordingly: to about eighteen times the margin if the surround lies midway between background and threshold, and to about seven times if it lies at four-fifths of the margin. Even the least demanding of these is far outside the observed distribution, whose intra-urban standard deviation at 100 m is 2.08 °C, so the conclusion holds; but the margin is narrower than the cold-surround figure implies. The informative pattern is the progression across percentiles, from 49 % to 37 % to zero, which shows that the property governing survival is patch size relative to cell size rather than temperature alone.

Three limits bound this analysis. Exceedance of a fixed threshold is not the same as detectability: a coarse field may fail to exceed a fine-grid threshold while still ranking the same locations highest. The analysis therefore bears on threshold exceedance alone. At 1 km the retained area is quantised in units of one cell, so the resolution of the retention statistic is about ±1 km^2, which matters most for the 99th-percentile row where the reported value is zero. And the reference population defining the percentile thresholds is the set of urban pixels carrying valid data in the composite concerned, whose area of approximately 450 km^2 is about a tenth smaller than the 503 km^2 of built-up land; the three percentile levels agree on that figure, so the exceedance statistics are internally consistent.

5.5 A residual difference remains between products on a common grid

Placing the two products on a common 1 km grid separates the component attributable to nominal grid size from everything else that differs between them (Eqs. 4–7). The residual difference between products on the identical grid averaged 1.24 °C in absolute value across individual months. That figure is numerically equal to the daytime SUHI intensity measured at 100 m, so under this comparison the discrepancy that remains after grid size has been equalised is the same size as the signal being measured. We take that absolute statement, rather than any ratio, as the result.

The grid-size component itself averaged 0.21 °C in absolute value across months and +0.02 °C for the seasonal composites, giving a ratio ρ = 5.9 (Fig. 5b; Table 3). This ratio should be treated with caution and is not used as a headline. Block-averaging preserves the area-weighted mean of a field over a fixed set of cells, so when the urban and rural sets are held fixed and cells tile the domain completely the class means are unchanged and Δ_{grid} is zero by construction; the small values observed arise only from incomplete cells at class boundaries and from unequal cell weights. A ratio whose denominator is driven toward zero in this way is not a stable summary, its magnitude can be increased simply by improving grid alignment, and no interval is attached to it. The defensible content of the comparison is that the residual is large in absolute terms, not that it is 5.9 times something small.

The residual is not an instrument effect. It contains, unseparated, the differences in overpass time, platform composition, retrieval algorithm, emissivity treatment, atmospheric correction, quality screening, viewing geometry and valid-acquisition availability listed in Section 4.4. Its seasonal structure is consistent with that compound character: the largest single monthly difference, 3.61 °C, occurred at monsoon onset in June 2020, when acquisition conditions and cloud screening differ most between the products, and pixel-level agreement on the common grid fell from r = 0.86 in the 2025 composite to r = 0.25 in June 2020. A low correlation between two measurements of the same surface indicates a loss of spatial correspondence rather than a calibration offset, and identifies monsoon-transition months as the period in which cross-product comparison is least reliable. No part of the residual is attributed to the instrument itself, since the design does not separate the contributing terms.

Table 3. Attenuation of the thermal field under aggregation, and partition of the Landsat–MODIS difference into a grid-size component and a residual on a common 1 km grid (Eqs. 4–7). Retention fractions use thresholds fixed at their 100 m values (Eq. 9). The first four rows are all evaluated at 1 km and are therefore comparable in support, although the grid-size term is a mean over the seasonal composites while the exceedance terms are for 2025 alone; the two rows at 2.9 km are shown for context and are discussed in Section 5.4. The residual is not an instrument effect; its composition is given in Section 4.4. Confidence intervals were not computed for these quantities, and retained areas at 1 km are quantised in units of about 1 km^2.

Quantity	Value	Interpretation
Mean SUHI intensity, 100 m → 1 km	+1.24 °C; change of +0.02 °C	Mean unchanged to within 2 % at 1 km (epoch-averaged)
Hot-surface area > 90th percentile, 100 m → 1 km	45 → 21.9 km^2 (49 % retained)	About half survives
Hot-surface area > 95th percentile, 100 m → 1 km	22 → 8.2 km^2 (37 % retained)	About a third survives
Hot-surface area > 99th percentile, 100 m → 1 km	4.5 → 0.0 km^2 (0 % retained)	Tail removed at the same support at which the mean is preserved

Quantity	Value	Interpretation
Extent and fragmentation of the hottest 1 % at 100 m	4.5 km^2 across 158 patches; mean patch ≈ 3 pixels	Patch size, not temperature alone, governs survival
Mean SUHI intensity, 100 m → 2.9 km	+1.24 → +0.79 °C (64 % retained)	Decline beyond 1 km; mechanism unresolved
Intra-urban standard deviation, 100 m → 2.9 km	2.08 → 1.40 °C (67 % retained)	Reported at 2.9 km only
Pure grid-size component, seasonal composites (mean)	+0.02 °C	Expected near zero by construction (Section 4.4)
Pure grid-size component, monthly (mean absolute)	0.21 °C	Reference magnitude for a tenfold change in pixel size
Residual product difference, monthly (mean absolute)	1.24 °C	Equal to the daytime SUHI intensity measured at 100 m
Ratio ρ = ⟨|Δresidual|⟩ / ⟨|Δgrid|⟩	5.9	Reported for completeness; denominator is near zero by construction
Largest single monthly discrepancy	3.61 °C (June 2020)	Monsoon onset; overpass and cloud handling diverge
Pixel agreement on the common grid	r = 0.86 (2025 composite); r = 0.25 (June 2020)	Loss of spatial correspondence, not a calibration offset

5.6 Amplitude of the anomaly and the ranking of daytime and night-time surfaces

Measured outward from the urban-core edge, the core ran +4.66 °C above the far-field background at night and +1.44 °C above it by day (Fig. 6), the nocturnal amplitude being 3.2 times the daytime one. This ratio is not the same quantity as the night-to-day ratio of 2.5 reported in Section 5.1: the latter contrasts all built land with all non-built land, whereas this one contrasts the contiguous core with the far field, and the two geometries need not give the same figure.

Under the fixed absolute criterion of Eq. (11) the night profile reaches within 0.5 °C of background at about 9 km and the day profile at about 12 km. These distances are not comparable as reported, for two reasons. The threshold is a different fraction of each amplitude, 35 % by day against 11 % at night, so the criterion is far more demanding after dark. And the background itself is estimated as the mean of bands beyond 15 km, so it carries a sampling error that is not propagated into the crossing distance.

Expressing the profiles instead through an exponential decay length, for which $A \cdot \exp(-d/L)$ reaches 0.5 °C at the observed distances, gives $L \approx 11.3$ km by day and $L \approx 4.0$ km at night. On that reading the nocturnal anomaly is both substantially larger in amplitude and roughly three times more spatially concentrated. We flag this as unresolved rather than interpret it. Nocturnal anomalies are not generally expected to be more compact than daytime ones, and the night field is observed at 1 km while the day field is observed at 100 m, so the coarser observation is showing the sharper spatial decay, which is the opposite of what differences in support alone would produce. Three explanations are available and the present data do not separate them: a real concentration of nocturnal storage on the dense built core; an artefact of applying a first-crossing criterion to a daytime profile that is shallow, noisy and non-monotonic, with a local maximum just outside the core edge, so that the crossing distance is unstable under small perturbations; or a difference between the two periods in the far-field background against which each profile is referenced. The first-crossing criterion is the least robust element of this comparison, and the amplitudes rather than the crossing distances carry the interpretable content.

The hottest urban quintile by day and by night overlapped at a Jaccard index of 0.16, with 27 % of daytime hot-spot area also night-time hot-spot area, and the resident population located within the 90th-percentile night-time surfaces was 2.6 million against 0.6 million for the corresponding daytime surfaces. These figures must be read with the qualification stated in Section 4.5: the daytime mask derives from Landsat at 100 m and the night-time mask from MODIS at 1 km, so the comparison confounds spatial support with time of day, and a low overlap is expected on those grounds alone. We therefore treat the overlap statistics as an indication that the two observations rank different surfaces highly, and not as a quantitative measure of day–night congruence. A defensible value requires the recomputation on a matched grid described in Section 4.5.

The population figures likewise describe the resident population recorded within the mapped surface-temperature zones. They do not measure the number of people present at the overpass time, individual heat exposure, air temperature, indoor conditions or physiological heat stress.

5.7 Ward-scale configuration

Across the 48 wards of the Ahmedabad Municipal Corporation, mean surface temperature was 45.8 °C by day and 26.2 °C at night (Fig. 7; Table 4). The warmest wards by day were the eastern industrial estates, led by Odhav, and by night the dense wards of the historic walled city: Dariyapur, Khadia, Jamalpur and Gomtipur. The rank correlation between ward-mean daytime and night-time temperature was weak and not statistically significant (Spearman $\rho = -0.18$, 95 % CI −0.46 to +0.13, $p = 0.22$, $n = 48$). With 48 wards the interval excludes only strong positive association, so this result is compatible with anything from a moderate negative to a weak positive relationship and should not be read as evidence that the two rankings are unrelated. The comparison also uses fields of different spatial support and was not repeated at matched support.

Ward heat is spatially clustered (Fig. 8). Global Moran's I was +0.56 for daytime and +0.47 for night-time ward LST (both $p \le 0.001$, 9,999 permutations). Local analysis identified a daytime high–high cluster of eight wards in the eastern industrial belt (Odhav, Vastral, Ramol-Hathijan and neighbours) and a twelve-ward low–low cluster across the planned western wards, while the night-time high–high cluster of nine wards lay in the historic core and the four-ward low–low cluster in the southern and south-western periphery. The two maps display different spatial configurations. We do not claim that the daytime and night-time clusters are statistically different, since that would require a direct test on the day–night contrast rather than a comparison of two separately thresholded maps.

Ward-mean daytime LST was weakly and not significantly related to ward-mean greenness (Spearman $\rho = -0.10$, 95 % CI −0.39 to +0.21, $p = 0.49$), an interval wide enough to be uninformative. At this level of aggregation the wards are uniformly built, and the finer-scale vegetation association reported in the supplementary material is averaged away.

Table 4. Ward-scale summary for the 48 wards of the Ahmedabad Municipal Corporation, April–June 2025 composite. Daytime values derive from Landsat at 100 m and night-time values from MODIS at 1 km; the two fields differ in spatial support and the day–night comparisons in this table were not repeated at matched support. Rank-correlation intervals are Fisher z intervals on n = 48 wards. Permutation inference uses 9,999 conditional permutations under queen contiguity with false-discovery-rate control. No intervals were computed for the ward-mean temperatures.

Quantity	Daytime (Landsat, 100 m)	Night-time (MODIS, 1 km)	Notes
Ward-mean LST, all 48 wards	45.8 °C	26.2 °C	1.1 °C and 2.9 °C above the corresponding rural background
Warmest ward	Odhav, 48.0 °C	Dariyapur, Khadia, Jamalpur and Gomtipur, each near 28.1 °C	Eastern industrial estates by day; historic walled city by night
Rank correlation between ward daytime and night-time LST	$\rho = -0.18$ (95 % CI −0.44 to +0.11; $p = 0.22$)	—	Interval wide; compatible with moderate negative through weak positive association
Rank correlation between ward LST and ward NDVI	$\rho = -0.10$ (95 % CI −0.37 to +0.19; $p = 0.49$)	—	Uninformative at this level of aggregation
Global Moran's I	+0.56 ($p \le 0.001$)	+0.47 ($p \le 0.001$)	Ward heat is spatially clustered in both periods
Local clusters: high–high / low–low	8 / 12 wards	9 / 4 wards	Daytime high–high in the eastern industrial belt; night-time high–high in the historic core

6. Discussion

6.1 What the measurement analysis shows

The three questions posed in Section 1.3 admit reasonably clear answers. The secondary question of day-night ranking does not, for the reason given there.

The rural reference class is the dominant discretionary influence on the daytime estimate in this domain. A 3.03 °C range obtained by changing nothing but the class of land treated as rural is larger than the daytime intensity itself under any of those definitions, and it includes a change of sign. Any daytime SUHI value reported for a semi-arid city without specifying the reference class is therefore uninterpretable at the precision usually implied, and values from studies using different reference definitions should not be compared directly.

Aggregation attenuates bulk statistics and threshold exceedance at markedly different rates. About a third of the mean intensity and a third of the intra-urban standard deviation are lost at 2.9 km, whereas none of the area above the fine-grid 99th percentile survives at 1 km. Two limits on this comparison must be kept in view: the measures were evaluated at different supports, and exceedance of a fixed threshold is not the same as detectability, since a coarse field may fail to exceed a fine-grid threshold while still ranking the same locations highest. What follows is a recommendation to report threshold behaviour alongside bulk statistics when judging a product, not a demonstration that coarse products cannot locate warm areas.

Placing two products on a common grid leaves a residual several times larger than the grid-size component. This is the clearest practical implication of the study, and it is also the result most easily over-interpreted. What the analysis establishes is that, for this domain and season and under this particular comparison, differences between the Landsat and MODIS composites that are not attributable to nominal grid size were larger than the component that is. It does not establish that the instruments themselves disagree, because overpass time, platform composition, retrieval, screening and compositing were not separated.

The secondary question, whether daytime and night-time observations rank the same parts of the city, is not answered here. Both the pixel-level overlap statistic and the ward-scale rank correlation compare a 100 m daytime field with a 1 km night-time field, so each confounds time of day with spatial support, and the ward-level correlation is in any case too imprecise to be informative ($\rho = -0.18$, 95 % CI −0.44 to +0.11). The matched-support daytime field required to resolve this is constructed within the present analysis for the product comparison of Section 4.4, so the recomputation is available and is the single most valuable extension to this work. We make no claim on the question until it is done.

6.2 Relation to previous work on Ahmedabad

The city's diurnal SUHI behaviour has been documented over far longer records than the two seasons analysed here. Mohammad et al. (2019) reported, from sixteen years of MODIS observations, a negative summer daytime SUHI, positive nocturnal intensities of 1.8 °C in summer and 3.2 °C in winter, and supporting in-situ measurements from a 2018 field campaign; Mathew et al. (2022) reported day–night reversal in the association between LST and surface bareness over thirteen years (Table 5). The present study neither confirms nor extends those findings in the temporal dimension, and its two composites are a much weaker basis for statements about the city's thermal behaviour than the records already published.

The differences between our values and theirs are themselves informative about the measurement question. Where Mohammad et al. (2019) report a negative summer daytime intensity, our seasonal composite is positive; where they report 1.8 °C at night, we report 3.38 °C. Several documented sensitivities could contribute: the rural reference class, which we show moves the daytime estimate across a 3.03 °C range and which differs between the two studies; the urban delineation; the analysis period, sixteen years against two; and the platform and compositing rules of the MODIS products used. Our reference-class result is sufficient in magnitude to account for a sign difference of the size observed, which supports the interpretation Mohammad et al. offered for the negative daytime signal, but we have not reproduced their processing chain and cannot attribute the discrepancy to any single factor. This is itself an illustration of the incommensurability that Zhou D. et al. (2019) identified: two careful studies of the same city, using overlapping products, report daytime intensities of opposite sign, and the difference is plausibly definitional rather than physical.

Table 5. Previously published surface urban heat island results for Ahmedabad and for Indian cities, and the relation of the present study to each. Values in the third column are as reported by the cited authors.

Study	Data and period	Reported for Ahmedabad or Indian cities	Relation to the present study
Mohammad et al. (2019)	MODIS, 2003–2018, summer and winter, day and night; field campaign 2018	Mean negative SUHI in summer daytime; +0.4 °C winter daytime; +1.8 °C summer night-time; +3.2 °C winter night-time. Negative daytime signal	Establishes the diurnal pattern over a far longer record than the two seasons analysed here. The present study quantifies

Study	Data and period	Reported for Ahmedabad or Indian cities	Relation to the present study
		attributed to cropland turning to bare soil in the pre-monsoon rural surround	the sensitivity of the daytime estimate to the rural reference class that they identify as the cause (Section 5.3)
Mathew et al. (2022)	MODIS (Terra and Aqua) and Landsat, 2003–2015, three seasons, day and night	LST inversely related to vegetation index and directly to built-up index; positively related to bareness by day but inversely at night	Reports the day–night reversal in surface-parameter associations for this city. The corresponding associations, reported in Supplementary Section S2, are consistent with this and do not extend it
Mathew et al. (2018)	Diurnal surface temperature analysis across Indian cities	Diurnal surface temperature variation used to assess SUHI over Indian cities	National-scale context for the diurnal behaviour treated here as established background
Mohammad and Goswami (2021)	Indian cities across climatic zones, diurnal and seasonal	Diurnal and seasonal variation of SUHI intensity and its determinants quantified by climatic zone	Places Ahmedabad's semi-arid behaviour in a national classification; not re-examined here
Shastri et al. (2017)	India-wide MODIS, day and night	Daytime SUHI negative over most urban areas in pre-monsoon, positive at night	Consistent in direction with the reference-class dependence quantified in Section 5.3
Kumar and Mishra (2019)	Indian cities, MODIS, heatwave and reference periods	SUHI declines during heatwaves: day −0.3 ± 0.7 °C, night −0.3 ± 0.4 °C	Directionally consistent with the appearance of the May 2020 daytime cool island in the season with more ERA5 heatwave days; two seasons cannot test the relationship
Rasul et al. (2015)	Erbil, semi-arid, Landsat 8, dry-season daytime	Daytime urban cool island of 3.5–4.6 °C; LST correlated with brightness r = +0.75 and wetness r = −0.90	Comparable setting with a stronger daytime cool island, consistent with a desert rather than cultivated surround; also reports the brightness association discussed in Section 6.6

6.3 Comparison with other semi-arid and Indian settings

Against the wider literature the results sit unremarkably in direction and are informative mainly in magnitude. Rasul et al. (2015) measured a daytime urban cool island of 3.5–4.6 °C in semi-arid Erbil and identified surface wetness rather than greenness as the controlling variable; Lazzarini et al. (2013, 2015) documented inversion of the conventional pattern in desert cities of the United Arab Emirates; Haashemi et al. (2016) showed that the sign and strength of the contrast follow the seasonal moisture cycle. Ahmedabad's daytime cool island, where it appears at all, is weaker than these, which is consistent with a cultivated rather than a desert surround. Kumar and Mishra (2019) reported that Indian SUHI intensity declines during heatwaves; our two seasons differ substantially in ERA5 heatwave days, and the season with more heatwave days is the one in which the May daytime cool island appears, which is directionally consistent, though two seasons cannot test the relationship.

On the measurement side, Sobrino et al. (2012) established that resolution and overpass time both affect the evaluated SUHI and Hu and Brunsell (2013) that temporal aggregation does likewise. The present decomposition adds a magnitude for one partition of that problem in one domain, namely that the non-grid residual exceeded the grid-size component by roughly a factor of six under the comparison used.

6.4 Implications for reporting

Three recommendations follow. A reported SUHI should be accompanied by the reference class, the product and collection, the platform and overpass time, the compositing rule and gap treatment, and the lineage of the urban mask; each was shown here, or is known from the cited literature, to be capable of moving the estimate by an amount comparable to the estimate itself. Cross-product comparison should be conducted on a common grid so that the grid-size component can be separated, and the residual described as such rather than as an instrument effect. And monsoon-transition months are unsuitable for cross-product comparison in this climate, given the loss of pixel-level correspondence observed in June 2020.

6.5 Relevance to heat planning, and its limits

Ahmedabad implemented South Asia's first municipal heat-health action plan following a 2010 heat event associated with a spike in all-cause mortality (Azhar et al., 2014; Knowlton et al., 2014), a plan subsequently associated with reduced mortality (Hess et al., 2018). Heatwave frequency has risen across India over recent decades (Rohini et al., 2016) and heatwave periods carry measurable increases in mortality risk (Mazdiyasni et al., 2017), so it is tempting to translate thermal results directly into targeting advice. We do so only weakly, because the analysis does not support more.

What the results indicate is that a monitoring programme relying on a single daytime, kilometre-scale composite would characterise the city differently from one using night-time observations, both in the wards it ranks highest and in the fine-scale surfaces it retains. Night-time temperature is relevant to heat-health outcomes on independent grounds, since impaired overnight recovery is an established component of heat-related mortality risk (Laaidi et al., 2012; Murage et al., 2017; Royé, 2017), within an epidemiology in which ambient temperature carries substantial attributable mortality (Gasparrini et al., 2015; Vicedo-Cabrera et al., 2021) and for which a broad portfolio of responses has been reviewed (Jay et al., 2021). Those results concern air temperature and human exposure, not land surface temperature.

That distinction is essential and we maintain it throughout. Land surface temperature is a radiometric skin temperature of the surfaces visible to a nadir-viewing sensor. It is not near-surface air temperature, not the heat index, and not human heat exposure, and the relationships among them are neither fixed nor spatially uniform (Venter et al., 2021; Nazarian et al., 2022). The population figures in Section 5.6 are counts of residents recorded within mapped surface-temperature zones, not measures of exposure. The ERA5 statistics are contextual meteorological evidence that one season was warmer than the other; they do not demonstrate that the satellite results represent human heat exposure. Nothing in this study identifies which populations are at risk, and the maps presented here should not be read as heat-risk maps.

Within those limits, the finding with the clearest planning relevance is the reference-class sensitivity, because it concerns how a monitoring indicator should be defined. A programme that tracks daytime SUHI against an unstated or drifting rural reference may register changes that originate in the reference rather than in the city.

6.6 Limitations

The limitations below are ordered by their consequence for the claims made. Each bounds an interpretation rather than qualifying a measurement, and the corresponding statements in Sections 5 and 7 are scoped accordingly.

Quantity measured. All thermal results are radiometric skin temperatures. They are not air temperature and not human exposure, and no health outcome is measured here.

Two composites, no temporal inference. The design supports a statement about two seasons. It cannot establish stability, reproducibility or trend, and none is claimed. The second composite functions as a check on the diurnal contrast, not as a second point in a series.

The residual product difference is compound. Overpass time, platform composition, retrieval algorithm, emissivity treatment, atmospheric correction, quality screening, viewing geometry and valid-acquisition availability are not separated. The magnitude reported here is therefore the combined effect of substituting one product for the other, and no component of it is attributed to the instrument. Resolving the overpass-time contribution in particular calls for diurnal-cycle information of the kind geostationary observation provides (Sismanidis et al., 2022).

Unmatched supports in the day–night comparisons. The pixel-level hot-spot overlap, the ward-level day–night comparison and the two regression models all involve a 100 m daytime field and a 1 km night-time field. Each therefore confounds time of day with spatial support, and none is interpreted quantitatively; they are reported because the direction they indicate is consistent across three independent measures, not because their magnitudes are meaningful.

Threshold exceedance is not detectability. The hot-tail result measures exceedance of a fixed fine-grid threshold, and complete loss at the 99th percentile is close to the arithmetically expected consequence of averaging surfaces whose mean patch is about three fine pixels. Whether the warmest locations remain identifiable at coarse support is a distinct question that this statistic does not address, and no claim is made about it.

Surface-property attribution is not presented as a finding. The regression of the thermal fields on surface descriptors is reported in the supplementary material rather than in the main text. Residual spatial autocorrelation is high, ordinary least squares does not represent it, and coefficient intervals, p-values, variance inflation factors and sample sizes are not available. The coefficients are accordingly described as descriptive associations within this domain and are not interpreted as identified effects.

Uncertainty is reported unevenly, and the degrees of freedom are modest. Confidence intervals are available for two of the SUHI estimates and for the two ward-level rank correlations. The grid-size and residual components, the dominance ratio, the retention fractions, the hot-spot areas, the population totals, the footprint distances, Cliff's delta and the difference between the two composites are reported as point values, so differences between them should not be read as statistically resolved unless the text states an interval. Where intervals do exist they rest on of order a hundred resampled tiles rather than on the pixel count, and the tile size is not calibrated against the correlation length of the field; both considerations make the reported intervals narrow rather than wide, and they are accordingly treated here as lower bounds on the sampling uncertainty.

The behaviour of the mean between 1 km and 2.9 km is unexplained. The mean intensity is preserved at 1 km and has lost a third of its value by 2.9 km. The most likely cause is progressive mixing of urban and rural land within coarse cells, which would mean that the decline measures degradation of the class mask rather than of the thermal field, but the fraction of mixed cells as a function of support was not computed and the question is open. Only the matched-support comparison at 1 km is unaffected.

The percentile reference population is not stated. The reported exceedance areas imply a reference population of about 450 km^2 rather than the nominal 503 km^2 of built-up land. The three percentile levels agree on that figure, so the analysis is internally consistent, but the pixel set defining the thresholds is not specified.

Population counts lack a denominator. The resident populations reported within the hot-spot zones are counts. The gridded population total for the domain and for the urban mask is not reported, so the counts cannot be converted into shares, which is the interpretable quantity.

Incomplete processing description. Product collection identifiers, per-month valid-acquisition counts, quality-flag settings, cloud-shadow screening rules and the exact provenance of the later-epoch urban mask are not reported, and are required for reproduction.

Clear-sky sampling. Compositing is conditioned on cloud-free acquisition. In June, when Landsat coverage falls to 94–96 %, the retained sample is a non-random subset of a monsoon-onset month.

Advection is unrepresented. The analysis treats each pixel's temperature as a function of local surface properties and omits horizontal heat transport, which has been shown to modify the apparent heat island of Indian cities (Dinda and Chatterjee, 2022).

Single city, two seasons. The results characterise one domain under one set of processing choices. We do not generalise them to semi-arid cities as a class; whether comparable sensitivities arise elsewhere is an open question that a multi-city analysis using a common processing chain could address.

7. Conclusions

This study asked how far a reported surface urban heat island intensity depends on decisions taken while measuring it, using Ahmedabad as the test domain. It is useful to separate what was observed, what depends on methodological choice, what remains a plausible but untested reading, and what the design does not establish.

Directly observed. In the 2025 hot-season composites the built area was 3.38 °C warmer than rural land at night (95 % CI 2.87–3.76) and 1.24 to 1.34 °C warmer by day, depending on the product. Holding epoch, product and season fixed and varying only the rural reference class moved the daytime estimate from −0.74 °C against bare ground to +2.29 °C against natural vegetation. At a common support of 1 km, aggregation left the mean intensity unchanged to within 2 % and retained none of the urban area exceeding the 99th percentile defined on the fine grid, the latter being a measure of threshold exceedance rather than of detectability. Extending the rescaling to 2.9 km reduced the mean to 64 % of its fine-grid value. With both products on a common 1 km grid, the residual monthly difference averaged 1.24 °C in absolute value, equal to the daytime intensity itself.

Dependent on methodological choice. The sign of the daytime intensity is determined by the rural reference class and by the month analysed rather than by the thermal field alone. Across twenty specifications the daytime estimate ranged from −0.7 to +2.6 °C while the night-time estimate remained between +2.8 and +3.9 °C. The apparent severity of aggregation loss depends on whether bulk statistics or threshold exceedance is used as the criterion. Complete loss of the 99th-percentile surface is, moreover, close to what block-averaging must produce given a mean patch of about three fine pixels, so that result measures fragmentation rather than a property of the product; how close depends on the temperature of the surround, which was not measured.

Plausible but untested. That the residual product difference arises substantially from overpass time and platform composition is consistent with its seasonal structure but was not tested. That the loss of mean intensity between 1 km and 2.9 km reflects mixing of urban and rural land within coarse cells is the most economical explanation but was not verified. That the nocturnal anomaly is genuinely more spatially concentrated than the daytime one, rather than the apparent difference arising from an unstable decay criterion, likewise remains open. That daytime and night-time observations identify different parts of the city is suggested by the ward-level rank correlation and the pixel-level overlap, but both comparisons use fields of different spatial support, and the ward-level correlation carries an interval (−0.44 to +0.11) too wide to exclude much of anything.

Not established by this design. The day–night comparisons rest on fields of unequal spatial support and therefore do not quantify hot-spot congruence between the two observations. The residual product difference is a compound quantity from which no instrument component is separated. The aggregation results measure exceedance of a fixed threshold and not the ability of a coarse product to locate the warmest surfaces. The surface-property associations reported in the supplementary material are descriptive within this domain and are not identified effects. Two composites cannot speak to temporal persistence, and no trend is inferred from them. Each of these bounds marks a place where a stronger reading of the numbers would not be warranted; none of them qualifies the measurements themselves.

The practical implication is narrow but firm. Surface urban heat island values are not comparable between studies unless the rural reference class, the spatial support, and the product, platform and compositing rules are reported together, because each of these was shown here to move the estimate by an amount comparable to the estimate itself. For intra-urban applications, attenuation of the upper tail should be reported alongside that of the mean, since the two respond very differently to aggregation. Both recommendations concern how such measurements are described, and neither depends on the particular thermal behaviour of the city studied.

Data availability

All satellite and ancillary datasets used in this study are publicly available: Landsat 8 and 9 and MODIS land surface temperature through the USGS and NASA LP DAAC archives; ESA WorldCover through Zenodo (Zanaga et al., 2021, 2022); the JRC Global Surface Water dataset (Pekel et al., 2016); the Global Human Settlement Layer (Schiavina et al., 2023; Pesaresi and Politis, 2023); and ERA5 through the Copernicus Climate Data Store (Hersbach et al., 2020). Collection identifiers, compositing rules, quality-screening criteria and mask definitions are given in Sections 3 and 4, and Supplementary Table S1 consolidates every quantitative result reported in the main text.

References

1. Anderson, G.B., Bell, M.L., Peng, R.D., 2013. Methods to calculate the heat index as an exposure metric in environmental health research. Environ. Health Perspect. 121, 1111–1119. https://doi.org/10.1289/ehp.1206273
2. Anniballe, R., Bonafoni, S., Pichierri, M., 2014. Spatial and temporal trends of the surface and air heat island over Milan using MODIS data. Remote Sens. Environ. 150, 163–171. https://doi.org/10.1016/j.rse.2014.05.005
3. Anselin, L., 1995. Local indicators of spatial association—LISA. Geogr. Anal. 27, 93–115. https://doi.org/10.1111/j.1538-4632.1995.tb00338.x
4. Arnfield, A.J., 2003. Two decades of urban climate research: a review of turbulence, exchanges of energy and water, and the urban heat island. Int. J. Climatol. 23, 1–26. https://doi.org/10.1002/joc.859
5. Azhar, G.S., Mavalankar, D., Nori-Sarma, A., Rajiva, A., Dutta, P., Jaiswal, A., Sheffield, P., Knowlton, K., Hess, J.J., 2014. Heat-related mortality in India: excess all-cause mortality associated with the 2010 Ahmedabad heat wave. PLoS ONE 9, e91831. https://doi.org/10.1371/journal.pone.0091831
6. Bounoua, L., Zhang, P., Mostovoy, G., Thome, K., Masek, J., Imhoff, M., Shepherd, M., Quattrochi, D., Santanello, J., Silva, J., Wolfe, R., Toure, A.M., 2015. Impact of urbanization on US surface climate. Environ. Res. Lett. 10, 084010. https://doi.org/10.1088/1748-9326/10/8/084010
7. Caldas de Castro, M., Singer, B.H., 2006. Controlling the false discovery rate: a new application to account for multiple and dependent tests in local statistics of spatial association. Geogr. Anal. 38, 180–208. https://doi.org/10.1111/j.0016-7363.2006.00682.x
8. Chakraborty, T., Lee, X., 2019. A simplified urban-extent algorithm to characterize surface urban heat islands on a global scale and examine vegetation control on their spatiotemporal variability. Int. J. Appl. Earth Obs. Geoinf. 74, 269–280. https://doi.org/10.1016/j.jag.2018.09.015
9. Chakraborty, T., Lee, X., Ermida, S., Zhan, W., 2021. On the land emissivity assumption and Landsat-derived surface urban heat islands: a global analysis. Remote Sens. Environ. 265, 112682. https://doi.org/10.1016/j.rse.2021.112682
10. Chakraborty, T., Sarangi, C., Tripathi, S.N., 2017. Understanding diurnality and inter-seasonality of a sub-tropical urban heat island. Bound.-Layer Meteorol. 163, 287–309. https://doi.org/10.1007/s10546-016-0223-0

11. Chow, W.T.L., Brennan, D., Brazel, A.J., 2012. Urban heat island research in Phoenix, Arizona: theoretical contributions and policy applications. Bull. Am. Meteorol. Soc. 93, 517–530. https://doi.org/10.1175/BAMS-D-11-00011.1
12. Cliff, N., 1993. Dominance statistics: ordinal analyses to answer ordinal questions. Psychol. Bull. 114, 494–509. https://doi.org/10.1037/0033-2909.114.3.494
13. Clinton, N., Gong, P., 2013. MODIS detected surface urban heat islands and sinks: global locations and controls. Remote Sens. Environ. 134, 294–304. https://doi.org/10.1016/j.rse.2013.03.008
14. Dijkstra, L., Poelman, H., Veneri, P., 2019. The EU-OECD definition of a functional urban area. OECD Regional Development Working Papers 2019/11. OECD Publishing, Paris. https://doi.org/10.1787/d58cb34d-en
15. Dinda, A., Chatterjee, S., 2022. Assessing the local impacts of heat advection on urban heat islands in Kolkata Metropolitan Area. Urban Clim. 42, 101139. https://doi.org/10.1016/j.uclim.2022.101139
16. Duan, S.-B., Li, Z.-L., Li, H., Göttsche, F.-M., Wu, H., Zhao, W., Leng, P., Zhang, X., Coll, C., 2019. Validation of Collection 6 MODIS land surface temperature product using in situ measurements. Remote Sens. Environ. 225, 16–29. https://doi.org/10.1016/j.rse.2019.02.020
17. Ermida, S.L., Soares, P., Mantas, V., Göttsche, F.-M., Trigo, I.F., 2020. Google Earth Engine open-source code for land surface temperature estimation from the Landsat series. Remote Sens. 12, 1471. https://doi.org/10.3390/rs12091471
18. Gasparrini, A., Guo, Y., Hashizume, M., Lavigne, E., Zanobetti, A., Schwartz, J., Tobias, A., Tong, S., Rocklöv, J., Forsberg, B., et al., 2015. Mortality risk attributable to high and low ambient temperature: a multicountry observational study. Lancet 386, 369–375. https://doi.org/10.1016/S0140-6736(14)62114-0
19. Getis, A., Ord, J.K., 1992. The analysis of spatial association by use of distance statistics. Geogr. Anal. 24, 189–206. https://doi.org/10.1111/j.1538-4632.1992.tb00261.x
20. Gorelick, N., Hancher, M., Dixon, M., Ilyushchenko, S., Thau, D., Moore, R., 2017. Google Earth Engine: planetary-scale geospatial analysis for everyone. Remote Sens. Environ. 202, 18–27. https://doi.org/10.1016/j.rse.2017.06.031
21. Grover, A., Singh, R.B., 2015. Analysis of urban heat island (UHI) in relation to normalized difference vegetation index (NDVI): a comparative study of Delhi and Mumbai. Environments 2, 125–138. https://doi.org/10.3390/environments2020125
22. Haashemi, S., Weng, Q., Darvishi, A., Alavipanah, S.K., 2016. Seasonal variations of the surface urban heat island in a semi-arid city. Remote Sens. 8, 352. https://doi.org/10.3390/rs8040352
23. Hersbach, H., Bell, B., Berrisford, P., Hirahara, S., Horányi, A., Muñoz-Sabater, J., Nicolas, J., Peubey, C., Radu, R., Schepers, D., et al., 2020. The ERA5 global reanalysis. Q. J. R. Meteorol. Soc. 146, 1999–2049. https://doi.org/10.1002/qj.3803
24. Hess, J.J., Sathish, L.M., Knowlton, K., Saha, S., Dutta, P., Ganguly, P., Tiwari, A., Jaiswal, A., Sheffield, P., Sarkar, J., et al., 2018. Building resilience to climate change: pilot evaluation of the impact of India's first heat action plan on all-cause mortality. J. Environ. Public Health 2018, 7973519. https://doi.org/10.1155/2018/7973519
25. Hu, L., Brunsell, N.A., 2013. The impact of temporal aggregation of land surface temperature data for surface urban heat island (SUHI) monitoring. Remote Sens. Environ. 134, 162–174. https://doi.org/10.1016/j.rse.2013.02.022
26. Imhoff, M.L., Zhang, P., Wolfe, R.E., Bounoua, L., 2010. Remote sensing of the urban heat island effect across biomes in the continental USA. Remote Sens. Environ. 114, 504–513. https://doi.org/10.1016/j.rse.2009.10.008
27. Jay, O., Capon, A., Berry, P., Broderick, C., de Dear, R., Havenith, G., Honda, Y., Kovats, R.S., Ma, W., Malik, A., Morris, N.B., Nybo, L., et al., 2021. Reducing the health effects of hot weather and heat extremes: from personal cooling strategies to green cities. Lancet 398, 709–724. https://doi.org/10.1016/S0140-6736(21)01209-5
28. Keeratikasikorn, C., Bonafoni, S., 2018. Satellite images and Gaussian parameterization for an extensive analysis of urban heat islands in Thailand. Remote Sens. 10, 665. https://doi.org/10.3390/rs10050665
29. Knowlton, K., Kulkarni, S.P., Azhar, G.S., Mavalankar, D., Jaiswal, A., Connolly, M., Nori-Sarma, A., Rajiva, A., Dutta, P., Deol, B., Sanchez, L., Khosla, R., et al., 2014. Development and implementation of South Asia's first heat-health action plan in Ahmedabad (Gujarat, India). Int. J. Environ. Res. Public Health 11, 3473–3492. https://doi.org/10.3390/ijerph110403473
30. Kumar, R., Mishra, V., 2019. Decline in surface urban heat island intensity in India during heatwaves. Environ. Res. Commun. 1, 031001. https://doi.org/10.1088/2515-7620/ab121d
31. Künsch, H.R., 1989. The jackknife and the bootstrap for general stationary observations. Ann. Stat. 17, 1217–1241. https://doi.org/10.1214/aos/1176347265

32. Laaidi, K., Zeghnoun, A., Dousset, B., Bretin, P., Vandentorren, S., Giraudet, E., Beaudeau, P., 2012. The impact of heat islands on mortality in Paris during the August 2003 heat wave. Environ. Health Perspect. 120, 254–259. https://doi.org/10.1289/ehp.1103532
33. Lahiri, S.N., 2003. Resampling Methods for Dependent Data. Springer Series in Statistics. Springer, New York. https://doi.org/10.1007/978-1-4757-3803-2
34. Lazzarini, M., Marpu, P.R., Ghedira, H., 2013. Temperature-land cover interactions: the inversion of urban heat island phenomenon in desert city areas. Remote Sens. Environ. 130, 136–152. https://doi.org/10.1016/j.rse.2012.11.007
35. Lazzarini, M., Molini, A., Marpu, P.R., Ouarda, T.B.M.J., Ghedira, H., 2015. Urban climate modifications in hot desert cities: the role of land cover, local climate, and seasonality. Geophys. Res. Lett. 42, 9980–9989. https://doi.org/10.1002/2015GL066534
36. Li, J., Song, C., Cao, L., Zhu, F., Meng, X., Wu, J., 2011. Impacts of landscape structure on surface urban heat islands: a case study of Shanghai, China. Remote Sens. Environ. 115, 3249–3263. https://doi.org/10.1016/j.rse.2011.07.008
37. Li, Y., Zhou, B., Glockmann, M., Kropp, J.P., Rybski, D., 2021. Context sensitivity of surface urban heat island at the local and regional scales. Sustain. Cities Soc. 74, 103146. https://doi.org/10.1016/j.scs.2021.103146
38. Li, Z.-L., Tang, B.-H., Wu, H., Ren, H., Yan, G., Wan, Z., Trigo, I.F., Sobrino, J.A., 2013. Satellite-derived land surface temperature: current status and perspectives. Remote Sens. Environ. 131, 14–37. https://doi.org/10.1016/j.rse.2012.12.008
39. Liu, Z., Zhan, W., Bechtel, B., Voogt, J., Lai, J., Chakraborty, T., Wang, Z.-H., Li, M., Huang, F., Lee, X., 2022. Surface warming in global cities is substantially more rapid than in rural background areas. Commun. Earth Environ. 3, 219. https://doi.org/10.1038/s43247-022-00539-x
40. Malakar, N.K., Hulley, G.C., Hook, S.J., Laraby, K., Cook, M., Schott, J.R., 2018. An operational land surface temperature product for Landsat thermal data: methodology and validation. IEEE Trans. Geosci. Remote Sens. 56, 5717–5735. https://doi.org/10.1109/TGRS.2018.2824828
41. Manoli, G., Fatichi, S., Schläpfer, M., Yu, K., Crowther, T.W., Meili, N., Burlando, P., Katul, G.G., Bou-Zeid, E., 2019. Magnitude of urban heat islands largely explained by climate and population. Nature 573, 55–60. https://doi.org/10.1038/s41586-019-1512-9
42. Mathew, A., Khandelwal, S., Kaul, N., 2018. Analysis of diurnal surface temperature variations for the assessment of surface urban heat island effect over Indian cities. Energy Build. 159, 271–295. https://doi.org/10.1016/j.enbuild.2017.10.062
43. Mathew, A., Sarwesh, P., Khandelwal, S., 2022. Investigating the contrast diurnal relationship of land surface temperatures with various surface parameters represent vegetation, soil, water, and urbanization over Ahmedabad city in India. Energy Nexus 5, 100044. https://doi.org/10.1016/j.nexus.2022.100044
44. Mazdiyasni, O., AghaKouchak, A., Davis, S.J., Madadgar, S., Mehran, A., Ragno, E., Sadegh, M., Sengupta, A., Ghosh, S., Dhanya, C.T., Niknejad, M., 2017. Increasing probability of mortality during Indian heat waves. Sci. Adv. 3, e1700066. https://doi.org/10.1126/sciadv.1700066
45. Mohammad, P., Goswami, A., 2021. Quantifying diurnal and seasonal variation of surface urban heat island intensity and its associated determinants across different climatic zones over Indian cities. GIScience Remote Sens. 58, 955–981. https://doi.org/10.1080/15481603.2021.1940739
46. Mohammad, P., Goswami, A., Bonafoni, S., 2019. The impact of the land cover dynamics on surface urban heat island variations in semi-arid cities: a case study in Ahmedabad city, India, using multi-sensor/source data. Sensors 19, 3701. https://doi.org/10.3390/s19173701
47. Murage, P., Hajat, S., Kovats, R.S., 2017. Effect of night-time temperatures on cause and age-specific mortality in London. Environ. Epidemiol. 1, e005. https://doi.org/10.1097/EE9.0000000000000005
48. Nazarian, N., Krayenhoff, E.S., Bechtel, B., Hondula, D.M., Paolini, R., Vanos, J., Cheung, T., Chow, W.T.L., de Dear, R., Jay, O., Lee, J.K.W., Martilli, A., et al., 2022. Integrated assessment of urban overheating impacts on human life. Earth's Future 10, e2022EF002682. https://doi.org/10.1029/2022EF002682
49. Oke, T.R., 1982. The energetic basis of the urban heat island. Q. J. R. Meteorol. Soc. 108, 1–24. https://doi.org/10.1002/qj.49710845502
50. Oke, T.R., Mills, G., Christen, A., Voogt, J.A., 2017. Urban Climates. Cambridge University Press, Cambridge. https://doi.org/10.1017/9781139016476
51. Pekel, J.-F., Cottam, A., Gorelick, N., Belward, A.S., 2016. High-resolution mapping of global surface water and its long-term changes. Nature 540, 418–422. https://doi.org/10.1038/nature20584
52. Peng, S., Piao, S., Ciais, P., Friedlingstein, P., Ottle, C., Bréon, F.-M., Nan, H., Zhou, L., Myneni, R.B., 2012. Surface urban heat island across 419 global big cities. Environ. Sci. Technol. 46, 696–703. https://doi.org/10.1021/es2030438

53. Pesaresi, M., Politis, P., 2023. GHS-BUILT-S R2023A – GHS built-up surface grid, derived from Sentinel-2 composite and Landsat, multitemporal (1975–2030). European Commission, Joint Research Centre. https://doi.org/10.2905/9F06F36F-4B11-47EC-ABB0-4F8B7B1D72EA
54. Pesaresi, M., Schiavina, M., Politis, P., Freire, S., Krasnodębska, K., Uhl, J.H., Carioli, A., Corbane, C., Dijkstra, L., Florio, P., et al., 2024. Advances on the Global Human Settlement Layer by joint assessment of Earth observation and population survey data. Int. J. Digit. Earth 17, 2390454. https://doi.org/10.1080/17538947.2024.2390454
55. Rao, P.K., 1972. Remote sensing of urban heat islands from an environmental satellite. Bull. Am. Meteorol. Soc. 53, 647–648.
56. Rasul, A., Balzter, H., Smith, C., 2015. Spatial variation of the daytime surface urban cool island during the dry season in Erbil, Iraqi Kurdistan, from Landsat 8. Urban Clim. 14, 176–186. https://doi.org/10.1016/j.uclim.2015.09.001
57. Rohini, P., Rajeevan, M., Srivastava, A.K., 2016. On the variability and increasing trends of heat waves over India. Sci. Rep. 6, 26153. https://doi.org/10.1038/srep26153
58. Roth, M., Oke, T.R., Emery, W.J., 1989. Satellite-derived urban heat islands from three coastal cities and the utilization of such data in urban climatology. Int. J. Remote Sens. 10, 1699–1720. https://doi.org/10.1080/01431168908904002
59. Royé, D., 2017. The effects of hot nights on mortality in Barcelona, Spain. Int. J. Biometeorol. 61, 2127–2140. https://doi.org/10.1007/s00484-017-1416-z
60. Schiavina, M., Freire, S., Carioli, A., MacManus, K., 2023. GHS-POP R2023A – GHS population grid multitemporal (1975–2030). European Commission, Joint Research Centre. https://doi.org/10.2905/2FF68A52-5B5B-4A22-8F40-C41DA8332CFE
61. Sekertekin, A., Bonafoni, S., 2020. Land surface temperature retrieval from Landsat 5, 7, and 8 over rural areas: assessment of different retrieval algorithms and emissivity models and toolbox implementation. Remote Sens. 12, 294. https://doi.org/10.3390/rs12020294
62. Shastri, H., Barik, B., Ghosh, S., Venkataraman, C., Sadavarte, P., 2017. Flip flop of day-night and summer-winter surface urban heat island intensity in India. Sci. Rep. 7, 40178. https://doi.org/10.1038/srep40178
63. Sismanidis, P., Bechtel, B., Keramitsoglou, I., Göttsche, F.-M., Kiranoudis, C.T., 2022. Satellite-derived quantification of the diurnal and annual dynamics of land surface temperature. Remote Sens. Environ. 265, 112642. https://doi.org/10.1016/j.rse.2021.112642
64. Sobrino, J.A., Oltra-Carrió, R., Sòria, G., Bianchi, R., Paganini, M., 2012. Impact of spatial resolution and satellite overpass time on evaluation of the surface urban heat island effects. Remote Sens. Environ. 117, 50–56. https://doi.org/10.1016/j.rse.2011.04.042
65. Steadman, R.G., 1979. The assessment of sultriness. Part I: a temperature-humidity index based on human physiology and clothing science. J. Appl. Meteorol. 18, 861–873. https://doi.org/10.1175/1520-0450(1979)018<0861:TAOSPI>2.0.CO;2
66. Stewart, I.D., Oke, T.R., 2012. Local climate zones for urban temperature studies. Bull. Am. Meteorol. Soc. 93, 1879–1900. https://doi.org/10.1175/BAMS-D-11-00019.1
67. Sultana, S., Satyanarayana, A.N.V., 2023. Impact of land use land cover on variation of urban heat island characteristics and surface energy fluxes using WRF and urban canopy model over metropolitan cities of India. Theor. Appl. Climatol. 152, 97–121. https://doi.org/10.1007/s00704-023-04362-y
68. Venter, Z.S., Chakraborty, T., Lee, X., 2021. Crowdsourced air temperatures contrast satellite measures of the urban heat island and its mechanisms. Sci. Adv. 7, eabb9569. https://doi.org/10.1126/sciadv.abb9569
69. Vicedo-Cabrera, A.M., Scovronick, N., Sera, F., Royé, D., Schneider, R., Tobias, A., Astrom, C., Guo, Y., Honda, Y., Hondula, D.M., et al., 2021. The burden of heat-related mortality attributable to recent human-induced climate change. Nat. Clim. Change 11, 492–500. https://doi.org/10.1038/s41558-021-01058-x
70. Voogt, J.A., Oke, T.R., 2003. Thermal remote sensing of urban climates. Remote Sens. Environ. 86, 370–384. https://doi.org/10.1016/S0034-4257(03)00079-8
71. Wan, Z., 2014. New refinements and validation of the collection-6 MODIS land-surface temperature/emissivity product. Remote Sens. Environ. 140, 36–45. https://doi.org/10.1016/j.rse.2013.08.027
72. Weng, Q., Fu, P., Gao, F., 2014. Generating daily land surface temperature at Landsat resolution by fusing Landsat and MODIS data. Remote Sens. Environ. 145, 55–67. https://doi.org/10.1016/j.rse.2014.02.003
73. Xia, H., Chen, Y., Song, C., Li, J., Quan, J., Zhou, G., 2022. Analysis of surface urban heat islands based on local climate zones via spatiotemporally enhanced land surface temperature. Remote Sens. Environ. 273, 112972. https://doi.org/10.1016/j.rse.2022.112972
74. Yang, C., Zhao, S., 2023. Diverse seasonal hysteresis of surface urban heat islands across Chinese cities: patterns and drivers. Remote Sens. Environ. 294, 113644. https://doi.org/10.1016/j.rse.2023.113644

75. Zakšek, K., Oštir, K., 2012. Downscaling land surface temperature for urban heat island diurnal cycle analysis. Remote Sens. Environ. 117, 114–124. https://doi.org/10.1016/j.rse.2011.05.027
76. Zanaga, D., Van De Kerchove, R., Daems, D., De Keersmaecker, W., Brockmann, C., Kirches, G., Wevers, J., Cartus, O., Santoro, M., Fritz, S., Lesiv, M., Herold, M., et al., 2022. ESA WorldCover 10 m 2021 v200. Zenodo. https://doi.org/10.5281/zenodo.7254221
77. Zanaga, D., Van De Kerchove, R., De Keersmaecker, W., Souverijns, N., Brockmann, C., Quast, R., Wevers, J., Grosu, A., Paccini, A., Vergnaud, S., Cartus, O., Santoro, M., et al., 2021. ESA WorldCover 10 m 2020 v100. Zenodo. https://doi.org/10.5281/zenodo.5571936
78. Zhan, W., Chen, Y., Zhou, J., Wang, J., Liu, W., Voogt, J., Zhu, X., Quan, J., Li, J., 2013. Disaggregation of remotely sensed land surface temperature: literature survey, taxonomy, issues, and caveats. Remote Sens. Environ. 131, 119–139. https://doi.org/10.1016/j.rse.2012.12.014
79. Zhao, L., Lee, X., Smith, R.B., Oleson, K., 2014. Strong contributions of local background climate to urban heat islands. Nature 511, 216–219. https://doi.org/10.1038/nature13462
80. Zhou, B., Rybski, D., Kropp, J.P., 2017. The role of city size and urban form in the surface urban heat island. Sci. Rep. 7, 4791. https://doi.org/10.1038/s41598-017-04242-2
81. Zhou, D., Xiao, J., Bonafoni, S., Berger, C., Deilami, K., Zhou, Y., Frolking, S., Yao, R., Qiao, Z., Sobrino, J.A., 2019. Satellite remote sensing of surface urban heat islands: progress, challenges, and perspectives. Remote Sens. 11, 48. https://doi.org/10.3390/rs11010048
82. Zhou, D., Zhao, S., Liu, S., Zhang, L., Zhu, C., 2014. Surface urban heat island in China's 32 major cities: spatial patterns and drivers. Remote Sens. Environ. 152, 51–61. https://doi.org/10.1016/j.rse.2014.05.017

Figures

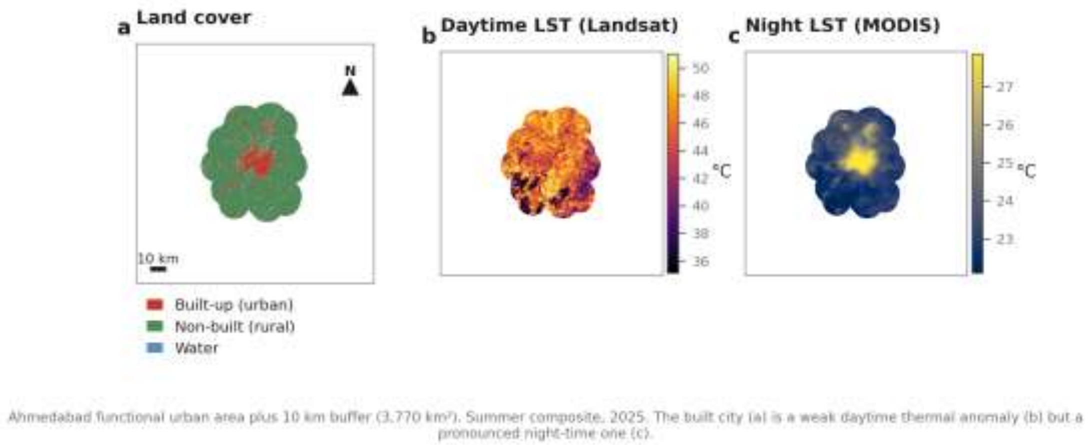

Fig. 1. Study area and thermal fields, April–June 2025 composite. (a) Land-cover classification of the analysis domain, the Ahmedabad functional urban area plus a 10 km buffer (3,770 km^2), showing built-up, non-built and water classes; (b) daytime land surface temperature, Landsat, 100 m; (c) night-time land surface temperature, MODIS, 1 km. Colour scales differ between (b) and (c) because the two fields occupy different temperature ranges. The night-time panel is shown at its native 1 km support. These are surface temperature fields and should not be read as heat-risk maps.

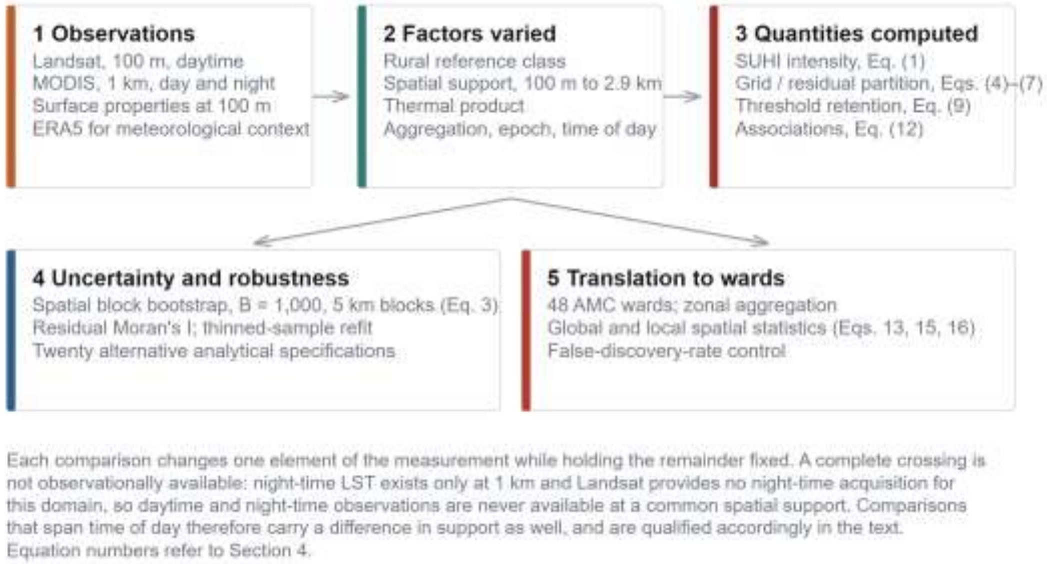

Fig. 2. Analytical workflow. Each comparison changes one element of the measurement while holding the remainder fixed. Daytime and night-time observations are not available at a common spatial support, so comparisons spanning time of day carry a difference in support as well; these are qualified in the text. Equation numbers refer to Section 4.

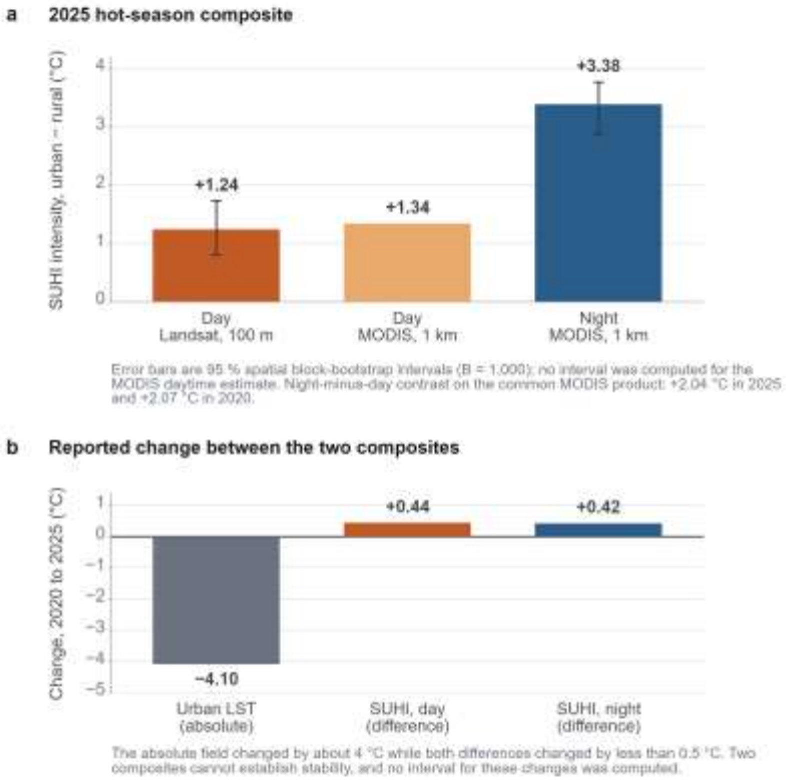

Fig. 3. Diurnal contrast in the 2025 composite and reported change between composites. (a) SUHI intensity, April–June 2025, for Landsat daytime (100 m), MODIS daytime (1 km) and MODIS night-time (1 km). Error bars are 95 % spatial block-bootstrap intervals (B = 1,000); no interval was computed for the MODIS daytime estimate. (b) Reported change between the 2020 and 2025 composites in the absolute urban daytime field and in the two differential quantities. No interval was computed for these changes, and two composites cannot establish temporal stability.

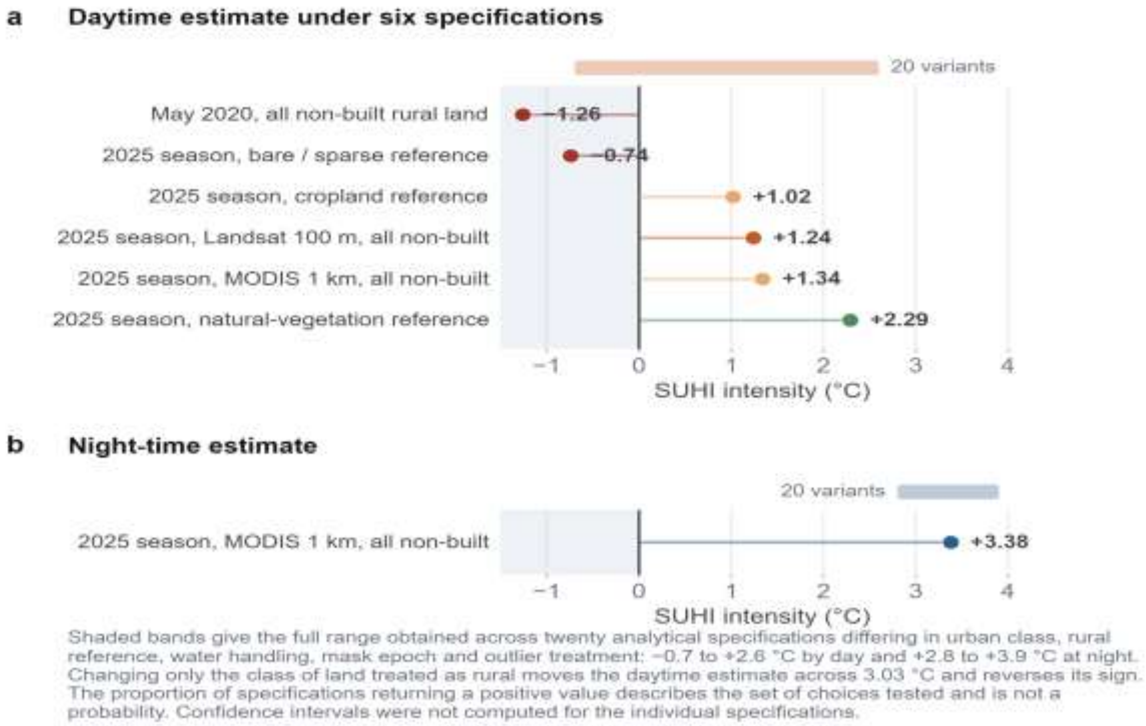

Fig. 4. Dependence of the estimate on the rural reference class and on analytical choice. (a) Daytime SUHI intensity under six specifications differing in the month analysed, the epoch, the thermal product or the class of rural land used as reference; (b) night-time intensity for the 2025 composite. Shaded bands give the full range across twenty analytical specifications (Section 5.3). Confidence intervals were not computed for the individual specifications.

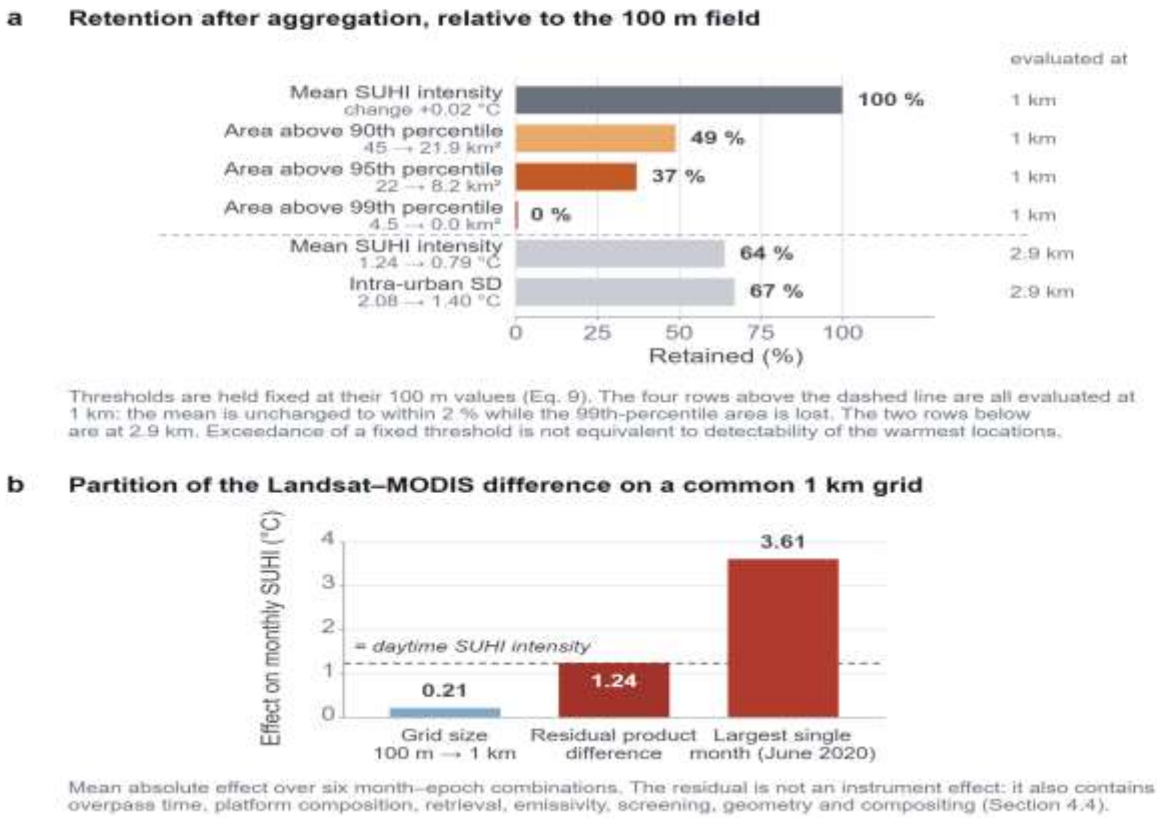

Fig. 5. Attenuation under aggregation and partition of the two-product difference. (a) Fraction of each quantity retained relative to its value on the 100 m Landsat field, with the support at which each was evaluated shown at right; thresholds are held fixed at their 100 m values (Eq. 9). The four quantities above the dashed line are

evaluated at 1 km: the mean intensity is unchanged to within 2 % while the area above the fine-grid 99th percentile is lost. The grid-size term is a mean over the seasonal composites and the exceedance terms are for 2025, so the two are matched in support but not in epoch. The two below are evaluated at 2.9 km. Retained area at 1 km is quantised in units of about 1 km^2. Exceedance of a fixed threshold is not equivalent to detectability of the warmest locations. (b) Mean absolute effect on the monthly SUHI over six month–epoch combinations of changing nominal grid size with the product held fixed, and of the residual difference between products on a common 1 km grid (Eqs. 4–7). The grid-size component is expected to be near zero by construction, so the ratio of the two is not used as a result; the residual is not an instrument effect, and its composition is given in Section 4.4. No intervals were computed for these components.

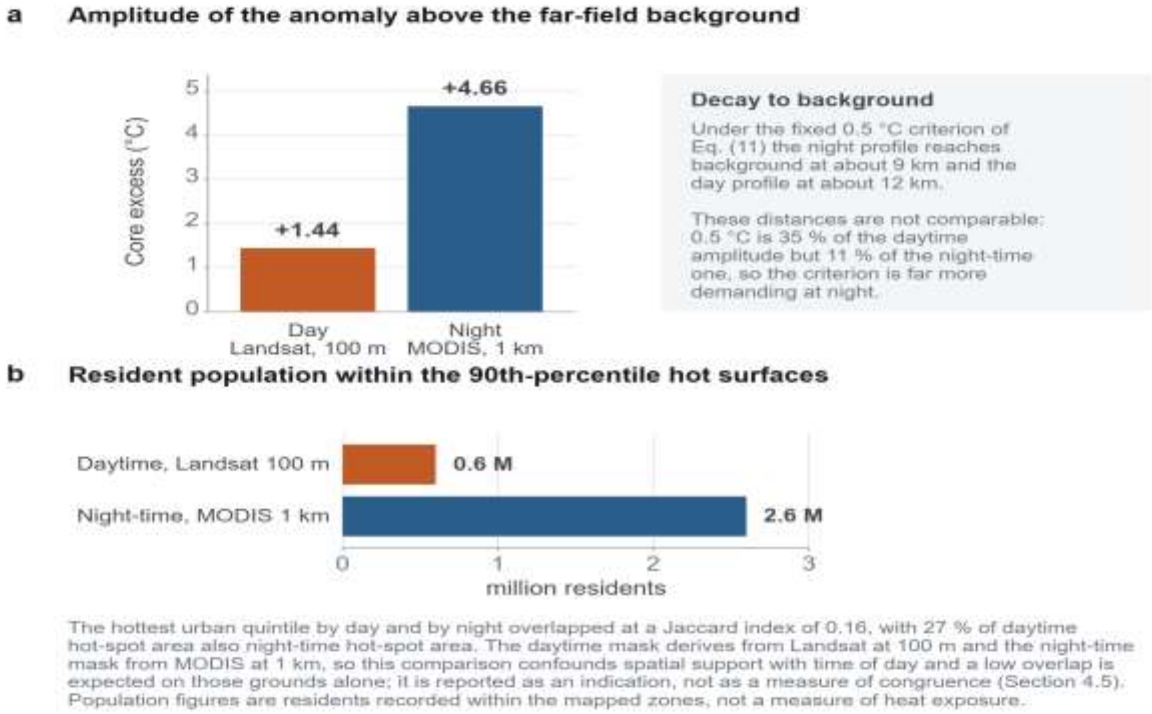

Fig. 6. Anomaly amplitude and the ranking of daytime and night-time surfaces. (a) Excess of the contiguous urban core over the far-field background, being the mean of distance bands beyond 15 km, for Landsat daytime (100 m) and MODIS night-time (1 km), April–June 2025. Decay distances under the fixed 0.5 °C criterion of Eq. (11) are not comparable between day and night because the threshold represents a different fraction of each amplitude. (b) Resident population recorded within the 90th-percentile hot surfaces of each period. The daytime and night-time masks differ in spatial support, so the overlap statistics quoted are indicative only (Section 4.5). Population figures are residential counts, not measures of heat exposure. No intervals were computed.

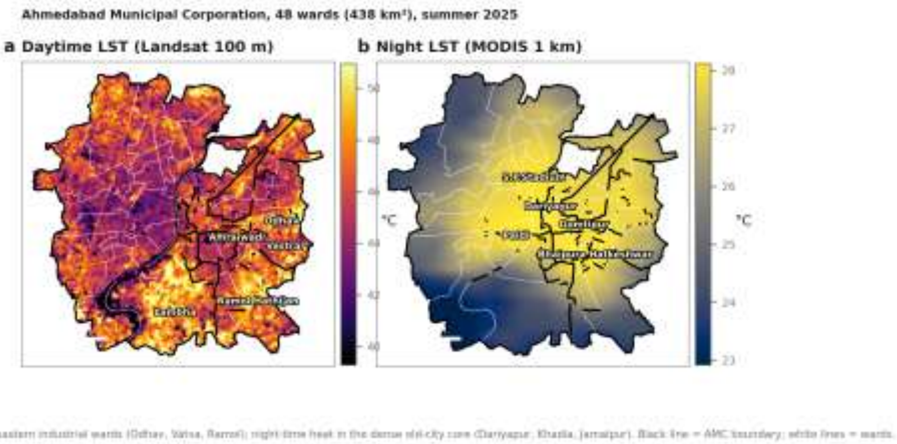

Fig. 7. Daytime and night-time surface temperature across the 48 wards of the Ahmedabad Municipal Corporation (438 km^2), April–June 2025 composite. (a) Landsat, 100 m, daytime; (b) MODIS, 1 km, night-time. Black line, municipal boundary; white lines, ward boundaries. The apparent smoothness of (b) reflects the 1

km native support of the night-time product displayed on the 100 m analysis grid. The two panels differ in spatial support and are not directly comparable. These are surface temperature fields, not heat-risk maps.

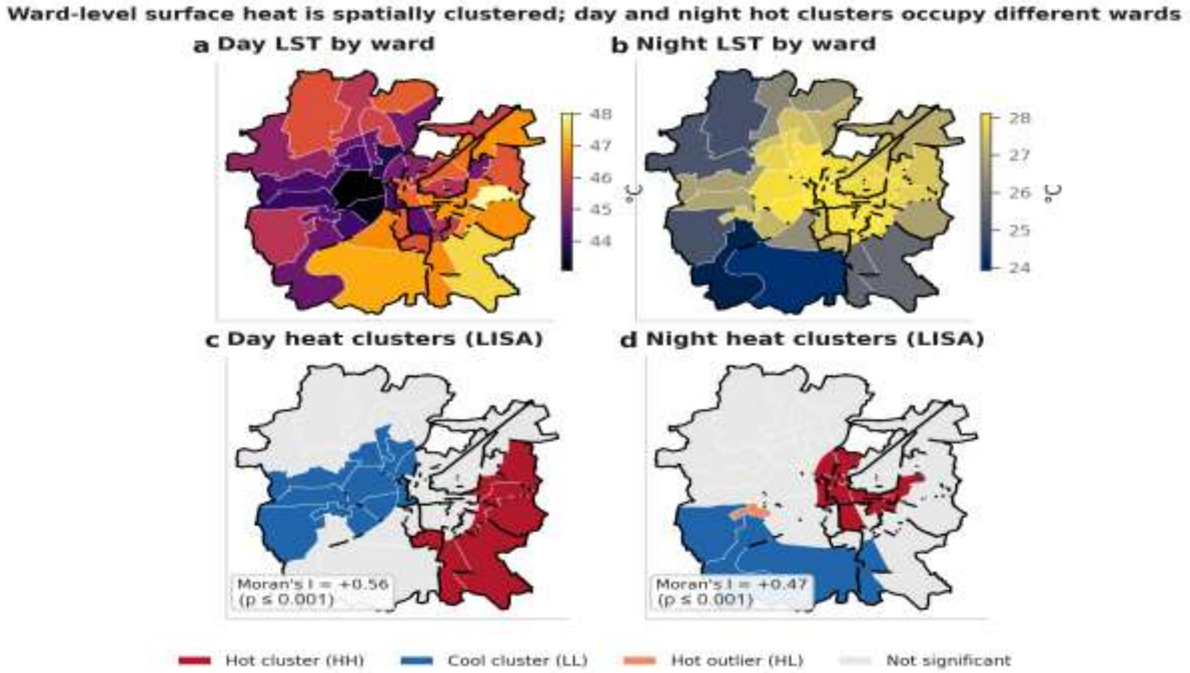

Fig. 8. Ward-scale spatial configuration, April–June 2025 (n = 48 wards). Choropleths of (a) daytime (Landsat, 100 m) and (b) night-time (MODIS, 1 km) ward-mean land surface temperature; local indicators of spatial association for (c) day and (d) night, classified from 9,999 conditional permutations under queen contiguity with false-discovery-rate control ($p \leq 0.001$ for the global statistics). The two maps display different spatial configurations; this is not a test of whether the daytime and night-time clusters differ, which would require a direct test on the day–night contrast. The two fields differ in spatial support.